

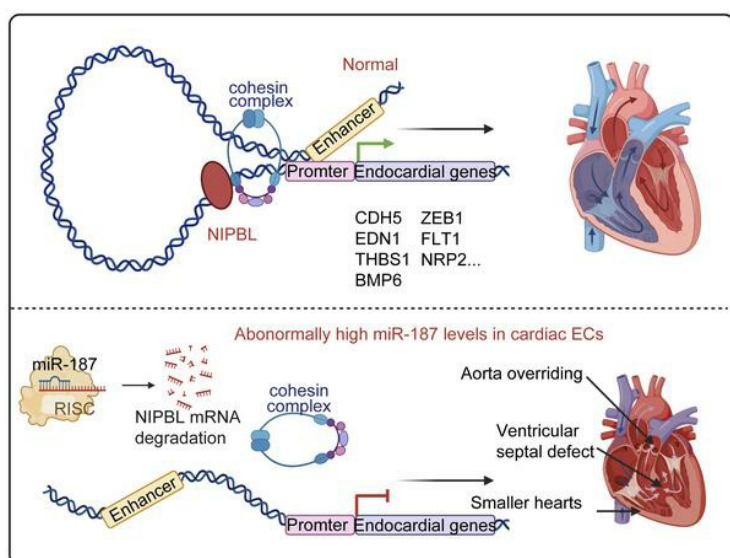
# Elevated microRNA-187 causes cardiac endothelial dysplasia to promote congenital heart disease through inhibition of NIPBL

Chao Li, ... , Jianfeng Shen, Hongyan Wang

*J Clin Invest.* 2024. <https://doi.org/10.1172/JCI178355>.

Research In-Press Preview Cardiology Development

## Graphical abstract



Find the latest version:

<https://jci.me/178355/pdf>



---

**Elevated microRNA-187 causes cardiac endothelial dysplasia to promote congenital heart disease through inhibition of NIPBL**

Chao Li <sup>1,2,#</sup>, Zizheng Tan <sup>2,#</sup>, Hongdou Li <sup>1,2</sup>, Xiaoying Yao <sup>1</sup>, Chuyue Peng <sup>1,2</sup>, Yue Qi <sup>1,2</sup>, Bo Wu <sup>3</sup>, Tongjin Zhao <sup>2</sup>, Chentao Li <sup>4</sup>, Jianfeng Shen <sup>5,\*</sup> and Hongyan Wang <sup>1,2,3,\*</sup>

1. Obstetrics and Gynecology Hospital, State Key Laboratory of Genetic Engineering, Children's Hospital, Fudan University, Shanghai 200438, China.

2. Shanghai Key Laboratory of Metabolic Remodeling and Health, Institute of Metabolism and Integrative Biology, Fudan University, Shanghai 200438, China

3. Prenatal Diagnosis Center of Shenzhen Maternity & Child Healthcare Hospital, Shenzhen 518028, China

4. Shanghai Medical College, Fudan University, Shanghai 200032, China

5. Department of Ophthalmology, Ninth People's Hospital, Shanghai JiaoTong University School of Medicine, Shanghai, 200025 China.

# These authors contributed equally.

\*Correspondence should be addressed to Hongyan Wang (wanghy@fudan.edu.cn) and Jianfeng Shen (jfshen@shsmu.edu.cn), Tel. & Fax: 86-21-31246611

---

## Abstract

Cardiac endothelial cells are essential for heart development, and disruption of this process can lead to congenital heart disease (CHD). However, how miRNAs influence cardiac endothelial cells in CHD remains unclear. This study identified elevated miR-187 expression in embryonic heart endothelial cells from CHD fetuses. Using a conditional knock-in model, we showed that increased miR-187 levels in embryonic endothelial cells induce CHD in homozygous fetal mice, closely mirroring human CHD. Mechanistically, miR-187 targets *NIPBL*, which is responsible for recruiting the cohesin complex and facilitating chromatin accessibility. Consequently, the endothelial cell-specific upregulation of miR-187 inhibited NIPBL, leading to reduced chromatin accessibility and impaired gene expression, which hindered endothelial cell development and ultimately caused heart septal defects and reduced heart size both in vitro and in vivo. Importantly, exogenous miR-187 expression in human cardiac organoids mimicked developmental defects in the cardiac endothelial cells, reversible by NIPBL replenishment. Our findings establish the miR-187/NIPBL axis as a potent regulator that inhibits cardiac endothelial cell development by attenuating the transcription of numerous endothelial genes, with our mouse and human cardiac organoid models effectively replicating severe defects from minor perturbations. This discovery suggests that targeting the miR-187/NIPBL pathway could offer a promising therapeutic approach for CHD.

---

36 **Brief summary**

37 MiR-187 upregulation in fetal cardiac endothelial cells induces CHD, mirroring human cases.

38 Mechanistically, miR-187 targets *NIPBL*, impairing chromatin accessibility and gene

39 expression critical for cardiac endothelial cells development. This study unveils the potent

40 regulatory role of the miR-187/NIPBL axis in CHD pathogenesis.



---

## 41 Introduction

42 Congenital heart disease (CHD), the most prevalent congenital disorder in newborns (1),  
43 includes ventricular septal defects (VSDs) as the predominant form, accounting for  
44 approximately 50% of cases. Among VSDs, the perimembranous subtype constitutes  
45 approximately 75% (2, 3). Tetralogy of Fallot (TOF), a severe form of CHD commonly featured  
46 with VSDs (3), serves as a valuable model for studying perimembranous VSDs. Previous  
47 research has identified more than 50 gene mutations (4) and de novo copy number variants  
48 (5) associated with specific types of CHD. However, over 55% of CHD cases remain unexplained  
49 (6). In particular, the genetic factors identified for perimembranous VSDs account for only a  
50 small subset of the cases (7), leaving a substantial gap in our understanding that warrants  
51 further investigation.

52  
53 In addition to gene mutations, related protein dosage alterations also regulate gene  
54 expression. MicroRNAs (miRNAs), short noncoding RNAs, typically interact with the 3'UTR of  
55 target mRNAs, leading to the suppression of protein production and playing a vital role in  
56 regulating post-transcriptional gene expression in both physiological and pathological  
57 processes of the heart (8). Given their established involvement in various aspects of cardiac  
58 development and disease, miRNAs are considered potential pathogenic factors in  
59 perimembranous VSDs(9).1

60  
61 During heart septum formation, a specific subset of cardiac endothelial cells (ECs) located  
62 above the future septum undergoes a transformation, giving rise to cardiac cushions. Cardiac

---

endothelial cell dysplasia, defined by impaired differentiation and function, can lead to underdeveloped cardiac cushions, potentially causing congenital heart defects in the valves and atrial septa (10). Several functional miRNAs associated with VSDs have been identified (11), and a few miRNAs in cardiomyocytes have been shown to induce VSDs in transgenic models and cardiomyocyte-specific (12) knockout mouse models (13, 14). In both mouse and human hearts, endothelial cells make up approximately 20-40% of the cellular composition (15, 16). Genes expressed in endothelial cells, such as JAG1 (17), play a critical role in heart development, particularly in septal formation. Nevertheless, our understanding of the physiological functions of endothelial-specific miRNAs in cardiac septal development is limited.

A recent comprehensive single-cell analysis of cardiogenesis has revealed an intriguing connection between CHD and altered chromatin accessibility specifically in the endothelium (18). Cohesin, a ring-shaped protein complex that attaches to chromosomes, plays a critical role in chromatin accessibility and remodeling, bringing regulatory DNA into close proximity with target DNA (19) and facilitating the folding of the genome into DNA loops (20). Cohesin-mediated loop extrusion and dwell time are essential for determining the positions of replication origins during mitosis (21). During interphase, cohesin contributes to shaping the genome into a three-dimensional structure and interacts with other regulatory factors to control gene expression (22). In the cohesin loading process, the Nipped-B-homolog (NIPBL) is important as a recruiting center (23). Haploinsufficiency of NIPBL due to mutations accounts for approximately 70% of cases of Cornelia de Lange syndrome (CdLS) (24, 25), an inheritable

---

disorder predominantly associated with cardiac septal defects (25). CHD is observed in 14-70% of individuals with CdLS (26, 27), often involving VSDs and atrial septal defects (ASDs), accompanied by hypoplastic ventricles (28). Recent studies revealed that 77% of *NIPBL*<sup>+/-</sup> mouse hearts displayed incomplete or completely absent contact between the developing ventricular septum and the cardiac cushion with smaller ventricles than those of wild type (WT) mice. However, the specific lineage responsible for the increased risk of septal defects remains unclear (29). Therefore, the understanding in regulatory mechanisms of NIPBL and the role of NIPBL in cardiac endothelial cells development might be crucial and helpful.

In this study, we aimed to identify key miRNAs involved in the development of VSDs during cardiac development. For this purpose, we utilized human cardiac organoids, human embryonic stem cell (hESC)-derived endothelial lineage differentiation, mouse genetic models, and epigenomic and transcriptomic analyses. We investigated and revealed the functional and molecular mechanisms underlying the regulatory role of miR-187 in cardiac endothelial cells development. Consequently, our findings demonstrated a critical role for the miR-187/NIPBL signaling pathway in early cardiac endothelial cells differentiation, shedding light on the pathogenic mechanisms underlying CHDs associated with dysregulated miR-187 and attenuated NIPBL expression.

---

## Results

### **Cardiac endothelial cell-specific upregulation of miR-187 is positively associated with the development of TOF.**

The nonrestrictive perimembranous VSD was reported to be strongly associated with TOF (3). To identify miRNA involvement in perimembranous development, we performed data mining to identify differentially expressed miRNAs in the right ventricular outflow tract of patients with TOF from three datasets (GSE35490, GSE40128, and GSE36759). Three upregulated miRNAs (miR-187-3p, miR-222-3p, miR-499a-3p) and two discordant miRNAs, miR-30a-3p (up in GSE35490/36759, down in GSE40128) and miR-381-3p (up in GSE36759/40128, down in GSE35490), were identified in the overlapping TOF datasets. We measured the expression levels of the three upregulated miRNAs using right ventricle tissues from aborted fetuses with TOF (Table S1, n = 3 pairs). Only miR-187 (miR-187-3p, abbreviated as miR-187) and miR-222 showed significantly higher expression in the TOF cases than in the controls (Figure 1B, left).

Furthermore, cardiac endothelial cells from the collected right ventricles were isolated using CD144 (VE-Cadherin) MicroBeads and magnetic-activated cell sorting (MACS) (Figure 1C). MiR-187 was the only miRNA that was intensely upregulated in endothelial cells marked by CD144 positive but remained stable in CD144 negative cells (Figure 1B, right). Meanwhile, except for CD144-positive cells, miR-187 expression also showed no difference in other examined tissues, including the brain, kidney, lung, and liver, between fetuses with TOF and controls (Figure S1A). Notably, the levels of the most common endothelial markers, CD31 and

---

VWF, were dramatically lower in right ventricle wall tissues from the fetuses with TOF than in the normal controls (Figure 1, D and E). Together, these results suggested that both increased miR-187 levels in endothelial cells and reduced endothelial cells might be involved in CHD onset.

### **MiR-187 inhibits the development of normal cardiac endothelial cells.**

We examined miR-187 levels during normal embryonic development in vivo and investigated how highly expressed miR-187 impaired endothelial cell differentiation in vitro. Compared to the later stages of heart development (week 23), the expression level of miR-187 remains relatively low from week 5 to week 9, which is a critical window for human embryonic heart development, and then gradually increases based on the results of microarray analysis (Figure 2A, Figure S1B). Similarly, compared to E15.5, mouse miR-187 is low during the critical window of heart development (the E10.5 to E12.5) and subsequently increases in later stage of heart development (Figure 2B, Figure S1C). Additionally, a modified approach (Figure 2C) was used to test the expression of those TOF-related miRNAs in differentiation of human-induced pluripotent stem cell-derived endothelial cells (30). Unlike the initial expression and subsequent increase of miR-187 in human and mouse hearts, miR-187 expression gradually decreased during endothelial cell differentiation as determined by RT-qPCR analysis (Figure 2D, Figure S1D). These findings suggest that maintenance of low miR-187 expression during critical stages of heart development is essential for proper early embryonic cardiac endothelial cells development. Predictably, abnormally high miR-187 levels might disrupt cardiac endothelial cells development in the embryonic heart.

147

148 To investigate the effect of high levels of miR-187 on endothelial cell function, we constructed  
149 hESC line with stable overexpression exogenous miR-187 and verified the pluripotency of  
150 hESC (Figure S2, A and B). Flow cytometry results indicated that the number of endothelial  
151 cells (CD31 positive) was significantly decreased on Day 12 during hESC-EC differentiation in  
152 cells with stable miR-187 overexpression (Figure 2E).

153

154 Furthermore, gene set enrichment analysis (GSEA) in a human endothelial cell line (EA.hy926)  
155 revealed that the regulation of endothelial cell proliferation, epithelial to mesenchymal  
156 transition (EMT), and meiotic cell cycle vasculature development (FDR<0.25) were impaired in  
157 endothelial cells transfected with miR-187 compared to controls (Figure 2F, Figure S2, C-G).  
158 RT-qPCR verified that in EA.hy926 cells treated with exogenous miR-187, the pathway  
159 markers for endothelial cell proliferation, positive regulation of epithelial-to-mesenchymal  
160 transition, positive regulation of the meiotic cell cycle, and regulation of vasculature  
161 development were downregulated (Figure 2G). These findings suggest that abnormally high  
162 miR-187 expression levels might contribute to endothelial pathogenesis through impaired  
163 proliferation and differentiation in an early stage of heart development.

164

165 **Endothelial-specific miR-187 knock-in model mouse recapitulates the phenotype of**  
166 **human CHD.**

167 MiR-187 knock-in (KI) mice were conditionally generated using the *Tek* (*Tie2*) promoter to  
168 limit the expression of exogenous miR-187 specifically in endothelial cells (Figure S3A). MiR-

---

187 expression levels in the right ventricles of homozygous KI mice were approximately  
tenfold higher than those in controls (Figure 3A, left), similar to increased miR-187 expression  
in TOF patients compared to controls. The upregulated cardiac miR-187 was exclusively  
limited to the cardiac endothelial cells between KI/KI and KI/+ mice (Figure 3A, middle),  
showing no significant changes in the compared cardiomyocytes (Figure 3A, right). The  
embryonic lethality in the homozygous miR-187 KI mice on day 10 was revealed by the  
interbreeding mendelian ratio of 14:60:33 in KI/KI, KI/+, and +/+ offspring (Figure S3B).  
Anatomical analysis revealed that the hearts of homozygous and heterozygous miR-187 KI  
pups at P0 were smaller than those of WT pups (Figure 3B), although the size of the  
cardiomyocytes did not change (Figure S3C). The body weight of the miR-187-KI pups were  
significantly lower than that of the control pups (Figure 3C, Figure S3, D-F). Remarkably, the  
heart/ body weight ratio and heart weight dramatically decreased in KI/KI mice compared  
with WT mice (Figure 3, D and E, Table S2). These results indicate that the overexpression of  
endothelial-derived miR-187 prominently reduced heart weight in addition to reducing  
whole body weight in KI/KI pups. The ejection fraction and intraventricular septum which  
evaluated by echocardiography in miR-187-KI mice were significantly lower than WT mice  
(Figure 3, F-H). We examined the cardiac phenotype using hematoxylin-eosin (H&E) stained  
sections at P0.5 and found VSDs displayed in 6 of 15 miR-187 KI/KI mice (Figure 3, I-K) and  
2 of 12 KI/+ mice (Figure S3G); aorta overriding in 4 of 15 KI/KI mice (Figure 3L); thin  
myocardium layer in 5 of 15 KI/KI mice and 3 of 12 KI/+ mice (Figure 3H, Figure S3, H-N); and  
smaller hearts in 7 of 15 KI/KI mice and 3 of 12 KI/+ mice (Figure 3B). The number of cardiac  
endothelial cells undergoing mitosis indicated by the *pH3*<sup>+</sup> marker was also decreased in

---

KI/KI and KI/+ mice (Figure S3O). Consistent with the in vitro results (Figure 2E), the expression of CD31, a marker of endothelial cells, was also significantly reduced in the right ventricle of miR-187-KI mice compared to controls (Figure 3M). FACS analyzed the number of cardiomyocyte and endothelial cells in the heart tissues from P0.5 mice. The FACS analysis results showed that the proportion of endothelial cells in the heart tissues of miR-187-KI mice was significantly lower than that in wild controls, but the proportion of cardiomyocytes between miR-187 KI mice and wild control mice showed no significant difference (Figure 3N). Both the reduction in mitotic cardiac endothelial cells and decreased endothelial cell numbers exhibited in KI mice are similar to what was observed in CHD patients (18). These results demonstrate that embryonic endothelial-specific expression of exogenous miR-187 in mice could recapitulate the phenotypes of human CHD.

**Doxorubicin-induced upregulation of miR-187 inhibits the growth of human heart-forming organoids.**

Being a risk factor for CHD, doxorubicin can significantly induce the expression levels of miR-187 in the cardiomyocytes (31–33). Embryonic stem cell-induced human heart-forming organoids (HFOs) serve as a valuable in vitro model that can mimic CHD phenotypes caused by genetic and environmental factors (34, 35). HFOs can simulate the early stages of cardiac development in vitro and have various cell types, including endothelial cells (34). Therefore, we hypothesized that doxorubicin-treated HFOs would exhibit increased miR-187 expression and display heart defects like those in miR-187 KI mice. We engineered a three-dimensional HFOs through biphasic regulation of the WNT signaling pathway (34) (Figure S4A), comprising



---

a myocardial layer surrounded by an inner core of cardiac endothelial cells and encased by proepicardial outer layer anlagen (Figure S4, B-F). In doxorubicin-treated HFOs, miR-187 expression was significantly elevated compared to controls (Figure S5A). The addition of a miR-187 inhibitor restored miR-187 levels to normal (Figure S5A). Doxorubicin treatment inhibits the growth of HFOs, as evidenced by significantly reduced volume and area compared to the control group; however, supplementation with miR-187 inhibitor restores HFOs growth (Figure S5, B-D). Through immunofluorescence detection of pH3-positive cells, doxorubicin-treated HFOs demonstrate markedly diminished mitotic capability compared to the control group (Figure S5E). We found that doxorubicin treatment inhibits endothelial cell differentiation in CD31-labeled D10 HFOs (Figure S5F). Supplementation with a miR-187 inhibitor restores the mitotic capability of HFOs and enhances the differentiation of endothelial cells (Figure S5, E and F). These results indicate that elevated miR-187 expression in HFOs can pathologically simulate the cardiac phenotype observed in miR-187 KI mice (Figure 3B; Figure 3M).

#### ***NIPBL* is a target of miR-187 during cardiac endothelial cells development**

To search for miR-187 targets involved in the pathogenesis of CHD, we performed a bioinformatics analysis of the TargetScan database ([https://www.targetscan.org/vert\\_71/](https://www.targetscan.org/vert_71/)) and identified 21 genes containing conserved miR-187 target sites (Table S3). In the MGI mouse phenotypic database, 6 of 21 possible target genes showed CHD-related phenotypes in individual knockout mice. Together with the three previously reported miR-187 target genes, *DAB2* (36), *PTRF* (37), and *SMAD7* (38) (Figure 4A), the RT-qPCR results verified six

---

downregulated genes and three upregulated genes among a total of nine target genes (Figure 4B). *NIPBL* was the most significantly downregulated gene, which plays crucial roles in developing septal defects and functions coordinately in cohesin loading on chromatin and transcription signaling (39), so we finally selected *NIPBL* for further investigation. Bioinformatics analysis showed that miR-187 is conserved across multiple species, and the binding sequence of miR-187 in the 3'UTR of *NIPBL* is also conserved between mice and humans (Figure S6, A and B). We hypothesized that the upregulation of miR-187 expression overinhibited *NIPBL* expression to impair proper gene expression, ultimately contributing to CHD occurrence.

First, the luciferase reporter assays indicated that miR-187 binds directly to the 3'UTR of *NIPBL* (Figure 4, C and D). We also demonstrated through RNA-IP experiments that miR-187 binds to the 3'UTR of *NIPBL*, when *SMAD7* being a positive control and *GAPDH* being a negative control (Figure 4E). Then, the expression of endogenous *NIPBL* could be reduced in vitro by the expression of exogenous miR-187 at both the mRNA (Figure 4F) and protein levels (Figure 4G, up) as quantified by grayscale analysis (Figure 4G, down) in hESC-ECs. Moreover, RT-qPCR showed that *NIPBL* mRNA levels were significantly lower in the right ventricle of human fetuses with TOF than in control fetuses (Figure 4H). Meanwhile, such differences were not found in other parallelly compared tissues (Figure S6C). Exclusively, both the in vivo *NIPBL* mRNA and protein levels were significantly lower in heart endothelial cells from miR-187-KI mice than that in controls (Figure 4, I and J, Figure S6D). These results demonstrate that miR-187 directly targets and negatively regulates *NIPBL*.

---

### **The miR-187-NIPBL axis is critical for maintaining endothelial differentiation**

We created lentivirus-mediated knockdown of NIPBL expression in human stem cells (Figure S6E) to test whether the upregulation of miR-187/NIPBL or reduced NIPBL impairs endothelial differentiation from hESC-ECs. FACS results showed that the percentage of endothelial cells indicated by the CD31 marker markedly decreased with stable knockdown of NIPBL expression in hESC-ECs compared with that of the scramble control group (Figure 4K; Figure S6F). We overexpressed both miR-187 and NIPBL in embryonic stem cells and evaluated pluripotency (Figure S6, G and H). Consistently, the FACS results also showed that the percentages of CD31-positive cells in miR-187-hESC-ECs were significantly lower than those in miR-187/NIPBL-hESC-ECs which co-expressed both miR-187 and NIPBL (Figure 4L; Figure S6I). Overexpression of NIPBL was able to reverse the expression reduction of many key endothelial genes independently induced by exogenous miR-187 (Figure 4, M and N; Figure S7, A-D). Moreover, inhibition of miR-187 expression by a miR-187-specific inhibitor resulted in enhanced differentiation efficiency and mitotic capacity of hESC-ECs compared to the control group (Figure S8, A-D). These results strengthen the role of the miR-187-NIPBL axis in regulating endothelial cell development and mitotic.

To determine whether miR-187 mediates endothelial cell differentiation and mitosis in cardiac development via other target genes such as SMAD7, a member of the TGF-beta signaling pathway (38), we co-expressed SMAD7 into miR-187-overexpressing hESC-ECs. The results showed that SMAD7 could partially reverse the inhibition of miR-187 on endothelial cell

---

differentiation and mitosis (Figure S8, C and D), which was weaker than the recovery efficacy produced by overexpressed NIPBL (Figure S8, C and D). This suggests that *NIPBL* may be the main effector target of miR-187 in regulating endothelial cell development. Meanwhile, both arterial EC development genes, including *GJA5*, *HAND2*, and *ANXA1*, and venous endothelial genes *NR2F2* did not change in the mature stage of endothelial cells overexpressed with miR-187 (Figure S8, E and F), which coincided with the phenotype of no apparent defects in vascular development observed in miR-187-KI mice. Collectively, the above results demonstrate that the up-regulated miR-187 disturbs cardiac endothelial cells differentiation by inhibiting the expression of NIPBL.

#### **The miR-187/NIPBL axis inhibits endothelial cell migration and tube formation**

As suggested by the RNA-seq results that miR-187 repressed core gene expression for migration, epithelial to mesenchymal transition, and angiogenesis in endothelial cells (Figure 2F; Figure S9), we speculated that the functions related to these genes might be regulated by the miR-187/NIPBL axis. The results of wound healing assays indicated that the closure areas of the miR-187 groups were significantly smaller than those of the miR-187/NIPBL co-expressed controls, vice versa, the reduced miR-187 expression enhanced hESC-EC migration (Figure S10A). Western blot analysis showed that miR-187-hESC-ECs had lower N-cadherin levels compared to miR-NC-hESC-ECs (none-competitive miRNAs), indicating impaired mesenchymal differentiation, which could be reversed by NIPBL overexpression or by miR-187 inhibitors (Figure S10, B and C). Overexpression of miR-187 reduced the mRNA levels of the EMT signaling markers CD31 and CDH5 in mature endothelial cells (Figure 4N). During

---

heart development, endothelial cells generate mesenchymal cells with migratory and plastic properties via EMT, the primary source of coronary vascular ECs (40). Indeed, defects in angiogenesis and downregulated expression of angiogenesis-associated genes were found with miR-187 overexpression (Figure 2F). MiR-187 transfected hESC-ECs displayed the shorter tube length, reduced junction number, and impaired mesh area in the tube formation assay, which could be partially rescued by NIPBL supplementation or miR-187 inhibitors (Figure S10D). The above results emphasized NIPBL as a key target gene of miR-187 in regulating endothelial cell function. The results that miR-187/NIPBL axis inhibits endothelial cell migration and angiogenesis in vitro would help us interpret the etiology of endothelial-overexpressed miR-187 in vivo.

**Overexpression of NIPBL reverses the small heart phenotype induced by miR-187 in human heart-forming organoids.**

The use of human embryonic stem cells to induce differentiation of HFOs can avoid species differences and enable rapid gene editing (35). Therefore, we chose a HFOs model to test whether NIPBL supplement can reverse the miR-187 induced phenotype. HFOs stably expressing miR-187, miR-187/NIPBL, or scramble hESCs (Figure S2, A and B; Figure S6, G and H) was used to study the effects of miR-187 on cardiac endothelial cells development.

Morphologically, miR-187-HFOs grew and dilated significantly slower between Days 1 and 9 compared to the standard rate of growth and expansion maintained by the scramble-HFOs (Figure 5, A and B; Figure S11, A-L). NIPBL supplementation in miR-187-hESCs on

---

differentiation day 1 could recover the standard rate of growth and expansion (Figure 5, A and B; Figure S11, A-L). H&E staining showed that the area of miR-187-HFOs was smaller than that of both miR-187/NIPBL-HFOs and scramble-HFOs, while the latter two showed no significant change (Figure 5C).

Immunofluorescence results focused on the mitotic marker pH3 showed that expression of miR-187 significantly suppressed the mitosis of HFOs, while supplementation with NIPBL restored such suppressed proliferation (Figure 5D). Specifically, immunofluorescence shows that miR-187 inhibited the proliferation of endothelial cells which was rescued by the expression of NIPBL (Figure 5E). The immunofluorescence results indicated that the proportion of CD31-positive cells in miR-187-HFOs was substantially lower than that in miR-187/NIPBL-HFOs and in scramble-HFOs and the percentage of CD31-positive cells in the latter two did not change significantly (Figure 5F). These data identify the pathogenic effect induced by overexpression of miR-187 through attenuation of NIPBL.

### **MiR-187 affects chromatin accessibility and gene expression in cardiac endothelial cells**

RNA-seq results showed that compared to those of scramble cells or miR-187/NIPBL-hESC-ECs, downregulated genes in miR-187-hESC-ECs were represented in Gene Ontology (GO) terms of GSEA (FDR<0.25) and involved in endothelial cell migration, proliferation, differentiation, vascular endothelial growth factor signaling pathway, mesenchymal cell differentiation, heart morphogenesis, and cardiac septum development (Figure 6A; Figure S9). We identified a total of 208 target genes downregulated by up-regulated miR-187 which

---

were responsible for restricting cardiac endothelial cells growth (Figure 6A), of which 65 downregulated genes could be restored by NIPBL supplementation (Figure S12, A-C). To explore whether these genes are subject to NIPBL-mediated transcriptional regulation, we performed CUT&Tag-seq experiments of NIPBL compared to that of H3K27Ac as controls for the active promoter and enhancer regions in hESC-ECs (Figure S13, A-C). We detected widespread binding to the promoter and predominantly active enhancer regions (Figure S13, A and B). For comparison, we included genome-wide CUT&Tag-seq data for H3K27Ac in hESC-ECs, showing its preferential binding (Figure S13, A-C). After narrowing down the results from the shared binding region genes between NIPBL and H3K27Ac, we identified 29 differentially expressed cardiac endothelial cells development-associated genes that are transcriptionally regulated by the miR-187/NIPBL axis (Figure 6, B and C). Consistently, RT-qPCR results found that most of the 29 genes were downregulated in the cardiac endothelial cells of miR-187-KI mice compared with WT mice (Figure 6D).

To investigate the chromatin accessibility changes of genes regulated by the miR-187/NIPBL axis, we conducted assay for transposase-accessible chromatin with sequencing (ATAC-seq) on hESC-ECs overexpressing miR-187 or co-overexpressing miR-187/NIPBL hESC-ECs. Some critical genes showed decreased ATAC-seq peaks and RNA-seq peaks on miR-187 overexpressed hESC-ECs, which was restored upon supplementation with NIPBL (Figure 6E left); Such result was further confirmed by ATAC-qPCR (Figure 6E right) and RNA-qPCR (Figure S13D). The RNA-seq results showed that the gene expression levels positively correlated with the distribution of the ATAC-seq signal (Figure S13E). To verify the in vitro

---

results, we plotted the chromatin accessibility in Cd31-magnetic bead-labeled endothelial cells from the heart tissues at P0 mice. The overall accessibility across the genome was reduced in the cardiac endothelial cells of miR-187-KI mice (Figure S14A), and the top peaks that lost accessibility were enriched in the promoter region (Figure S14B). Predictably, the miR-187/NIPBL axis affected genome-wide chromatin accessibility and the actively transcribed development-related genes in cardiac endothelial cells were significantly impacted. The epigenomic landscape of cardiac endothelial cells in miR-187 KI mice was further compared to that in WT mice to reveal the miR-187-*NIPBL* axis regulation model in vivo. ATAC-seq results showed that the accessibility of some critical genes among the 29 genes was decreased in the miR-187-KI group compared to that in the control mice (Figure 6F). All the above findings prove that overexpression of miR-187 reduces the accessibility of chromatin, inhibits cardiac endothelial cells gene transcription, and provides molecular support for the observed phenotype of cardiac endothelial cells malformation (Figure 6G). Moreover, our zebrafish model suggests a critical role for miR-187 in CHD (Figure S15). Overall, these findings highlight miR-187's crucial role in disrupting chromatin accessibility and gene expression in cardiac endothelial cells, contributing to congenital heart disease.



---

## Discussion

MiR-187 plays essential roles in the control of cancerous cell proliferation, osteoblast (39, 40) and keratinocyte differentiation, and regulation of the immune response and insulin metabolism (41, 42). Here, we report a CHD mouse model created by cardiac endothelial cells specific overexpression of miR-187. Usually, the promoters *myh6* and *myh7* are used to drive cardiomyocyte-specific gene expression or deletion for CHD studies(43), (44), so CHD caused by endothelial cell abnormalities might be grossly underestimated, although nearly one-third of heart cells are endothelial either in humans or in mice (15, 17). Hence, our miR-187-KI mice provide a pioneer mouse model to elucidate miR-187-mediated regulation of cardiac endothelial cells and heart development.

NIPBL is needed to adequately load cohesin onto chromosomes, hop on chromosomal loops, and close target genes with distant regulatory factors to activate gene transcription (25), (45). The enrichment of *NIPBL* mutations was detected in patients with atrioventricular septal defect (AVSD) (46), and an inadequate dose of NIPBL resulted in defective heart development in mice (29). In this study, we identified miR-187 to be highly expressed in cardiac endothelial cells from TOF patients and showed miR-187 as a master regulator of NIPBL downregulation at the post-transcriptional level. Consequently, being the first identified regulator beyond *NIPBL* mutations, overexpressed miR-187 decreases the accessibility of endothelial development-related genes adjacent to chromatin by targeting *NIPBL*, which finally leads to incomplete endothelial development, septal defects, and smaller hearts.

---

Mutations in *NIPBL* are the most common cause of CdLS, with 60-70% of patients characterized by abnormal cardiac development, alongside anxiety-related behaviors and other malformations (47). *NIPBL* binding sites are enriched within the dysregulated gene's promoter region, and these genes expression are significantly reduced in CdLS-predisposed individuals due to *NIPBL* mutations. Our study suggests that overexpression of miR-187 produces pathological effects on cardiac development by targeting *NIPBL*, which could be restored by supplementing *NIPBL*. Despite miR-187 targeting multiple genes such as *SMAD7*, it was found that *NIPBL* might be the primary downstream effector of miR-187 specifically in endothelial cells. Our result also confirms that the cardiac developmental abnormalities caused by *NIPBL* dosage deficiency are mainly caused by excessive inhibition of genes related to cardiac endothelial development. Considering the mechanism of how *NIPBL* mutations in CdLS cause CHD, we provide a possible explanation that the shared dysregulation of endothelial development could be attributable to *NIPBL* mutations or miR-187-induced *NIPBL* downregulation. Additionally, no differences were observed in the open field test for miR-187 KI mice (Figure S16, A and B). In the light/dark transition test, although the frequency of transitions between the light and dark compartments remained unchanged (Figure S16C), miR-187 KI mice spent significantly more time in the dark compartment, indicating heightened anxiety-like behavior (Figure S16D). This suggests that miR-187 KI mice partially exhibit the anxiety phenotype seen in CdLS.

Given the human genomic background, the present HFOs employed in our study worked as a good in vitro model to recapitulate smaller hearts for studying developmental mechanisms,

---

function, and pathogenesis in a dish, providing insight into the nature of CHD and offering an ideal opportunity for potential high-throughput drug discovery for adult cardiopathy. We applied HFOs to demonstrate that miR-187-overexpressing HFOs exhibited slow growth reminiscent of the cardiac malformations observed in *NIPBL*-knockout mice (29). Subsequently, supplementation with NIPBL restored normal cardiac morphology both in miR-187-HFOs and in our miR-187-KI mice. These results suggest that targeting miR-187/NIPBL could be a promising therapeutic strategy for CHD. Additionally, the miR-187-mediated dysregulation of endothelial development resulting in CHD could be partially attributable to the inhibition of *NIPBL*. Our research sheds light on the role of miR-187/NIPBL signaling in controlling endothelial and cardiac development as potential therapeutic targets for the prevention of CHD.

#### **Limitation**

Although we found that doxorubicin can induce an increase in miR-187 expression in HFOs in vitro, showing a phenotype like miR-187 KI mice, the in vivo factors that trigger the upregulation of miR-187 in CHD cardiac endothelial cells have not yet been determined. Notably, circulating miR-187 in adults with hypertension-induced heart failure is highly expressed (48), indicating the dual function of miR-187 in both the developing heart and the functional adult heart.

---

## **Materials and Methods**

### **Sex as a biological variable**

Our study examined male and female animals, and similar findings are reported for both sexes.

### **Human tissue samples**

Our subjects were  $\approx$  20-week miscarried fetuses with nonsyndromic TOF ( $n = 5$ , i.e., no 22q11.2 deletion), and sex- and age-matched miscarried fetuses without TOF ( $n = 5$ ) were used as controls. The diagnosis was obtained by echocardiography and confirmed during an anomaly scan. Informed consent was obtained from a parent or legal guardian after reviewing the consent document and answering their questions. The right ventricle, brain, liver, lung, and kidney tissues were surgically excised from miscarried fetuses with TOF or control. All experiments involving this study were conducted with approval from the Medical Ethics Committee at the Obstetrics & Gynecology Hospital of Fudan University.

### **Endothelial cells MACS Separation**

Single-cell suspensions of human and mouse hearts were prepared through tissue mincing and enzymatic digestion using an isolation enzyme kit (Thermo Scientific, MA, USA, 88281). Human and mouse hearts were collected and minced into  $\approx$  1 mm blocks. Minced hearts were digested in 200  $\mu$ L Isolation Enzyme 1 and Isolation Enzyme 2 (Thermo Scientific, 88281) in HBSS (Thermo Scientific, 88281) at 37°C 30 min with tissue suspension triturated every 10 min. 500  $\mu$ L cold buffer 0.5% FBS (Corning, NY, USA, CGR-35-081-CV), 2 mM EDTA (Invitrogen,

---

MA, USA, AM9260G) in PBS (Gibco, MA, USA, 10010049)) was added to stop digestion and the resulting cell suspensions were filtered through a 40 µm cell strainer (Falcon, MA, USA, 352340) before centrifugation at 300 g for 5min at 4°C. Determine cell number and resuspend cell pellet in 80 µL of buffer per 10<sup>7</sup> total cells. Add 20 µL of *CD144* (*VE-Cadherin*) MicroBeads, human (Miltenyi Biotec, Bergisch Gladbach, North Rhine-Westphalia, Germany, 130-097-857) for human hearts or *CD31* MicroBeads, mouse (Miltenyi Biotec, 130-097-418) for mouse hearts. Mix well and incubate for 15 minutes at 4°C. Cells were washed by adding 1 mL buffer and centrifuged at 300 g for 5min at 4°C. For detection of positive cell rate, the cell pellet was resuspended in 500 µL buffer and added staining antibodies human CD31-APC (eBioscience, MA, USA, 17-0319-42) or mouse CD31-APC (eBioscience, 17-0311-82) before incubating for 15 min in the dark at 4°C. LS Columns were placed in MACS separator (Miltenyi Biotec, 130-042-303) and rinsing with 3×1 mL of buffer. The cell suspension was added to the column and washed with 3×1 mL of buffer before the magnetically labeled cells were flushed out by firmly pushing the plunger into the column.

### **Cardiomyocytes separation**

Collagenase II was used to dissociate mouse cardiac tissue at 37°C for 1 hour, followed by filtration through a 100 µm mesh to collect single-cell suspension. The suspension was treated with 1 mL of red blood cell lysis buffer at room temperature for 1 hour, centrifuged at 300g for 5 minutes to remove the supernatant, and subsequently incubated with 647 Mouse Anti-Cardiac Troponin T (BD Pharmingen, Woburn, MA, USA, 565744) PBS at 4°C for 30 min in the dark. Cardiac Troponin T-labeled cardiomyocytes were collected using the BD FACS Aria cell

---

sorter (BD Biosciences, Franklin Lakes, NJ, USA) and used for subsequent experiments.

#### **Real-time reverse transcription RT-qPCR and RNA-seq**

Cells or tissue samples were extracted using Trizol and isolated with a miRNeasy Mini Kit (Qiagen, Hilden, Germany; 217004) following the manufacturer's recommendations. For miRNA detection, 2 µg of total RNA was used to synthesize cDNA using a miRNA First-Strand cDNA Synthesis Kit (GeneCopoeia, Shanghai, China; QP014). RT-qPCRs were next performed in 96-well plates using a miRNA RT-qPCR Detection Kit (GeneCopoeia; QP016). For mRNA detection, 500 ng of total RNA was used to synthesize cDNA using a HiScript III 1st Strand cDNA Synthesis Kit (+gDNA wiper) (Vazyme, Nanjing, China, R312). The mRNA levels were determined by RT-qPCR using a HiScript III All-in-one RT supermix perfect for qPCR (Vazyme, R333). All RT-qPCRs were performed using the Applied Biosystems QuantStudio 1 Real-Time PCR System in a volume of 20 µL. Data were quantified using the comparative CT method, with U6 or *GAPDH* as reference genes. Relative gene expression levels were calculated using the  $2^{-\Delta\Delta CT}$  method. A list of the qPCR primers used in this study can be found in Table S4.

Human endothelial cells (EA.hy926), hESC-ECs, and cardiac endothelial cells from P0 neonatal KI/KI and WT control mice were collected for RNA-seq assay performed by BGI Genomics (Shenzhen, China) and APEX BIO (Shanghai, China) respectively.

#### **ATAC-seq and ATAC-qPCR**

To prepare the sample for ATAC-qPCR, 50,000 viable cells were pelleted at 500 RCF at 4°C

---

for 5 minutes, and the supernatant was aspirated. Next, 50  $\mu$ L of cold ATAC-Resuspension Buffer (RSB) containing 0.1% NP40, 0.1% Tween-20, and 0.01% Digitonin was added to the cell pellet and pipetted up and down three times. The mixture was then incubated on ice for 3 minutes, and the lysis was washed out with 1 mL of cold ATAC-RSB containing 0.1% Tween-20 but no NP40 or digitonin. The nuclei were pelleted at 500 RCF for 10 minutes at 4°C, and the supernatant was aspirated. The cell pellet was then resuspended in 50  $\mu$ L of transposition mixture (25  $\mu$ L 2x TD buffer, 2.5  $\mu$ L transposase (100 nM final), 16.5  $\mu$ L PBS, 0.5  $\mu$ L 1% digitonin, 0.5  $\mu$ L 10% Tween-20, 5  $\mu$ L H<sub>2</sub>O) by pipetting up and down six times. The reaction was incubated at 37°C for 30 minutes. The DNA was subsequently purified with the VAHTS DNA Clean Beads (Vazyme, N411-01 ) and amplified with barcode primers using the TruePrep DNA Library Prep Kit (Vazyme, TD501-01). Subsequent sequencing and data analysis were outsourced to APExBIO in Shanghai, China. ATAC-qPCR was performed using the same library construction method as in ATAC-seq. The ATAC libraries were subsequently adapted for RT-qPCR using specific primers designed based on the previous articles(49).

## **CUT&Tag**

The CUT&Tag assay used the Hyperactive Universal CUT&Tag Assay Kit for Illumina (Vazyme, TD903). In brief, 10<sup>5</sup> ECs were collected and washed with 500  $\mu$ L of wash buffer. The cells were then bound to ConA beads for 10 minutes at 25°C. Subsequently, the cells were incubated with 1  $\mu$ g of *NIPBL* (bethyl laboratories, Montgomery, Texas, A301-779A-T) or H3K27Ac (Abcam, ab177178) antibody at 4°C overnight. The next day, anti-rabbit IgG was added and incubated for 1 hour at 25°C. After three washes with DIG wash buffer, the cells were

---

incubated with 0.04  $\mu$ M pA/G-Tnp for 1 hour at 25°C. Following three washes with DIG 300 buffer, the cells were resuspended in tagmentation buffer and incubated at 37°C for 1 hour. Tagmentation was stopped by adding proteinase K, buffer LB, and DNA extract beads. The cells were then incubated at 55°C for 10 minutes, and the unbound liquid was removed after plating the cells on a magnet. The beads were gently rinsed twice with 80% ethanol, and the DNA was eluted with double-distilled water. Libraries were constructed using the TruePrep Index Kit V2 for Illumina (Vazyme, TD202). Subsequent sequencing and data analysis were outsourced to GENEWIZ Biotechnology Co., LTD (Suzhou, China).

#### **Cell culture**

Human embryonic stem cell line H9 (WA09, obtained from WiCell Research Institute, Madison, WI, USA) was cultured on Matrigel Matrix (1:200, Corning, 354277) pre-coated six-well plates at 10  $\mu$ g / cm<sup>2</sup> growth area in mTeSR1 medium plus (StemCell Technologies, Vancouver, Canada, 100-0276) in a humidified incubator at 37°C with 5% CO<sub>2</sub>. The cells were seeded at a density of 5 × 10<sup>5</sup> cells/well, and the medium was replaced every two days.

EA.hy926 and HEK293T cells were obtained from the ATCC and cultured in DMEM (Gibco, 11995073) with 10% fetal bovine serum (Corning, 35076111) and 1‰ Plasmocin (InvivoGen, San Diego, CA, USA; ant-mpt) at 37°C and 5% CO<sub>2</sub>.

hESC-ECs were cultured in gelatin-coated (Sigma Aldrich, G2500-100G) 6-well plates in EGM-2 Endothelial Cell Growth Medium-2 Bullet Kit (Lonza, Boston, MA, USA, CC-3162).



---

## Differentiation of human embryonic stem cell-derived endothelial cells

The protocol to generate endothelial cells from hESCs was modified from the previously reported method (30). Briefly, hESCs were seeded on Matrigel-coated plates in mTeSR1 medium plus to 30% confluency. At 30% confluency, the hESCs were pushed towards the mesodermal lineage by treatment of 6  $\mu$ M CHIR-99021 (Selleck, Houston, TX, USA; S1263) in Essential 6 (E6, Gibco, A1516401) medium for one day, followed by a non-treatment in E6 medium for one day. At day 2 of differentiation, the cells were subjected to a differentiation medium comprised of E6 medium supplemented with 300 ng/mL Recombinant Human VEGF (R&D Systems, Minneapolis, MN, USA, 293-VE-010/CF), 200 ng/mL Recombinant Human FGF-2 (Peprotech, MA, USA, 100-18B), 1 mM 8-Bromoadenosine 3',5'-cyclic monophosphate sodium salt monohydrate (8Bro, Sigma-Aldrich, St. Louis, MO, USA, 858463-25MG), and 50  $\mu$ M Melatonin (Sigma-Aldrich, M5250-1G) for 48 h. From day 4 to day 12, the culture medium was changed every 48 h into E6 medium supplemented with 10 ng/mL VEGF and 10 ng / mL bFGF, and 10  $\mu$ M hydrocortisone (Selleck, Houston, Texas, USA, S1696).

## Lentivirus infection

To produce pri-miR-187 and/or *NIPBL* expressing hESC-ECs, Human embryonic kidney (HEK) 293T cells were grown to 80% confluence on 100-mm plates. Co-transfection of 12  $\mu$ g of pLJM1-pri-miR-187 and/or PCDH-*NIPBL* with the packaging plasmids (7.8  $\mu$ g of pMDL, 6  $\mu$ g of pREV, and 4.2  $\mu$ g of pVSVG from Addgene) was carried out using Lipofectamine 2000 (Invitrogen; 11668019). After 48 hours, the viral supernatant was collected, concentrated using

---

PEG 8000, and stored at -80°C. hESCs were infected with the pri-miR-187 and/or *NIPBL* expressing lentivirus and then selected with puromycin (0.2 µg/mL, InvivoGen, ant-pr-1) for two weeks. RT-qPCR was performed to confirm the expression of miR-187 and *NIPBL*. The resulting hESC-ECs are pri-miR-187 and/or *NIPBL* expressing hESC-ECs.

### **Immunofluorescence staining**

Immunofluorescence staining was performed on hESC-ECs plated on Matrigel-coated glass-bottom dishes (Nest, Wuxi, China; 801001) or heart/HFO sections using a procedure previously described. The cells or heart sections were fixed and permeabilized with 0.5% Triton X-100 (Sangon, Shanghai, China, A110694-0100) in PBS for 5 minutes and then blocked with 5% BSA (Sangon, A600332-0100) in PBS for 1 hour at room temperature. The samples were incubated with primary antibodies diluted in 3% BSA blocking solution overnight at 4°C. The samples were then incubated with a secondary antibody and stained with DAPI. The slides were observed under a confocal microscope (Carl Zeiss LSM880).

### **Flow cytometry**

The pri-miR-187, pri-miR-187/*NIPBL* and scramble hESC-ECs were treated with StemPro Accutase Cell Dissociation Reagent (Gibco, A1110501) and incubated with APC-conjugated Mouse Anti-Human *CD31*(WM59) (Thermo Scientific, MA, USA, 17-0319-42) in PBS at 4°C for 30 min in the dark. Collagenase II was used to dissociate mouse cardiac tissue at 37°C for 1 hour, followed by filtration through a 100 µm mesh to collect single-cell suspension. The suspension was treated with 1 mL of red blood cell lysis buffer at room temperature for 1

---

hour, centrifuged at 300g for 5 minutes to remove the supernatant, and subsequently incubated with FITC-conjugated Rat Anti-Mouse *CD31* (WM59) (BD Pharmingen, Woburn, MA, USA, 553372) and 647 Mouse Anti-Cardiac Troponin T (BD Pharmingen, Woburn, MA, USA, 565744) PBS at 4°C for 30 min in the dark. The cells were then sorted using a BD FACSCalibur (BD Biosciences, Franklin Lakes, NJ, USA), and Gallios (Beckman Coulter, IN, USA). The resulting data were analyzed using FlowJo.

## **Mouse studies**

The experimental procedures followed the Administrative Panel on Laboratory Animal Care protocol and the institutional guidelines by the Medical Ethics Committee at the Obstetrics & Gynecology Hospital of Fudan University. Rosa26 site-specific mir-187-knockin mice, also known as mir-187-KI mice, were created using the CRISPR/Cas9 system on a C57BL/6J background. These mice expressed a single copy of exogenous mmu-mir-187, controlled by the mouse *Tek* (*Tie2*) promoter.

To prepare for microinjection, capped mRNAs for Cas9 were generated using the mMESSAGEmMACHINE in vitro transcription kit (Invitrogen, AM1344) following the manufacturer's instructions. The RNA's integrity was verified by electrophoresis on a 1% agarose gel after denaturation using the loading buffer provided in the Invitrogen kit. Standard plasmid DNA preparation was used, followed by extraction with phenol/chloroform (Sangon, PD0419-1). The DNA was then diluted to 10 ng/μL with sterile microinjection TE buffer (0.1 mM EDTA, 10 mM Tris, pH 7.5 (Solarbio, Beijing, China, T1140)) and stored at -80°

---

C until the injection. RNase-free DNA was ensured by incubating it with in vitro transcribed RNA at 37°C for one hour and analyzing the mix on a 1% agarose gel after denaturation using the loading buffer.

To generate Rosa26 (R26) site-specific mir-187-knockin mice, a donor plasmid containing a mouse mir-187 genomic fragment (5' –TCAGGCTACAACACAGGACCCGGGCGCTGCTCTGAC CCCTCGTGTCTTGTGTTGCAGCCGG– 3') and flanking region controlled by a *Tek* promoter, *Tek* enhancer, and a rabbit globin polyA signal sequence was constructed. The Cas9 mRNA and a single guide RNA (sgRNA) targeting the R26 locus were generated, and the donor vector, Cas9 mRNA, and sgRNA (5' –GGCAGGCTTAAAGGCTAACC– 3') were co-microinjected into fertilized eggs from C57BL/6J mice, which were then transferred to pseudopregnant mice. The injection mixes contained 5 ng/μL DNA and 50 ng/μL of in vitro transcribed Cas9 mRNA in microinjection TE buffer. Stable Mendelian transmission was confirmed, and RT-qPCR verified endothelial-specific expression of mmu-mir-187. The injection mixes were prepared before each injection by mixing equal volumes of 10 ng/μL DNA solution and 100 ng/μL mRNA solution.

To confirm the site-specific insertions in the animals, we conducted three PCR tests: one for the junction at the 5' end, one for the junction at the 3' end, and one located internally within the transgene. The genomic DNA from their offspring was analyzed to confirm positive homologous recombination by PCR. After obtaining the heterozygous miR-187-KI mice, we established homozygous mice by backcrossing them with wildtype C57BL/6J mice and self-

---

crossing the heterozygous mice. These lines were maintained by breeding homozygous animals and exhibited normal fertility.

#### **Echocardiographic studies**

Mice were maintained on a heating platform to keep their body temperature at 36.5-37.5°C. The mice were anesthetized with 2% isoflurane and then kept under mild anesthesia during the echocardiographic procedure. Cardiac ultrasound was performed using the Vevo770 imaging system. Initially, the long and short axes of the mouse heart were visualized in B-mode, followed by analysis of the short axis in M-mode.

#### **Open field test**

Each mouse was placed in a corner of the open field apparatus (40×40×30 cm) with an illumination level of 100 lux. The number of entries into the central area (20×20 cm) and the duration spent there were recorded over a 10-minute period.

#### **Light/dark transition test**

The light/dark transition test was conducted using a cage (21×42×25 cm) divided into two equal compartments by a partition with a door. One compartment was brightly lit (390 lux), while the other remained dark (2 lux). Mice were placed in the dark compartment and allowed to freely move between the two compartments for 10 minutes with the door open. Transition frequency and time spent in each compartment were recorded using ImageLD software.

---

## 666    **Histological analysis**

667    The hearts collected at E13.5 or P0 were fixed with 4% paraformaldehyde (pH 7.4, Sigma-  
668    Aldrich, P6148-1kg) for 30 or 50 minutes and then embedded in paraffin (Sangon, A606115).  
669    They were then sectioned at a thickness of 10 µm and subjected to Hematoxylin and Eosin  
670    (H&E) staining (Sangon, E607318-0200) for routine histological examination using a light  
671    microscope.

## 673    **Transfection**

674    The miRNA mimic (B02004) and miRNA inhibitor (B03004) were obtained from GenePharma  
675    (Shanghai, China) and used for transfection experiments. To purify endothelial cells,  
676    endothelial cells derived from hESCs were purified by MACS at least once, reaching a  
677    minimum purity of 90%. Transfection of miRNA mimic, miRNA inhibitor, siRNA, or negative  
678    control (NC) was carried out using Lipofectamine RNAiMAX (Invitrogen, Carlsbad, CA, USA,  
679    13778075), while co-transfection of miR-187 mimic and *NIPBL*-expressing plasmids was  
680    performed using Lipofectamine 3000 (Invitrogen; L3000015). Cells were collected 48 h after  
681    transfection.

## 683    **Antibodies**

684    Primary antibodies against the following proteins were used in this study: anti-*SOX2* Antibody  
685    (1:500 for IF, Cell Signaling Technology, Danvers, MA, USA, 3579T), anti-*GAPDH* Antibody  
686    (1:5000 for WB, Proteintech, Rosemont, USA, 60004-1), anti-human *CD31* (1:500 for IF,  
687    Abcam, ab9498), anti-mouse *CD31* (1:500 for IF, BD Pharmingen, 557355), anti-*Von*

---

688 *Willebrand Factor* (1:500 for IF, Abcam, ab6994), FITC-conjugated Mouse anti-Human  
689 *CD31*(WM59) (1:50 for FACS, BD Pharmingen, 557508), anti-human *CD31* (PECAM-1)  
690 Monoclonal Antibody, APC (1:50 for FACS, eBioscience, 17-0311-82), Wheat Germ Agglutinin,  
691 Alexa Fluor 488 Conjugate (1:500 for IF, Invitrogen, W11261), anti-*NIPBL* Antibody (1:1000  
692 for WB, 1:50 for CUT&TAG, bethyl laboratories, A301-779A-T), anti-Histone *H3* Antibody  
693 (1:1000 for WB, Cell Signaling Technology, 4499), anti-human Phospho-Histone *H3* (Ser10)  
694 Antibody (1:500 for IF, Cell Signaling Technology, 53348T), anti-mouse Phospho-Histone *H3*  
695 Antibody (1:500 for IF, Sigma-Aldrich, 06-570), anti- $\alpha$ -*Actinin* antibody (1:500 for IF, Sigma-  
696 Aldrich; A7732), anti-*WT1* antibody (1:500 for IF, Abcam, ab89901), anti-*NFAT2* antibody  
697 (1:500 for IF, Abcam, ab25916), anti-H3K27Ac antibody (1:50 for CUT&TAG, Abcam, ab177178)  
698 and anti-Normal Rabbit IgG (1:50 for CUT&TAG, Cell Signaling Technology, 2729)

699

700 The secondary antibodies were goat anti-rabbit Alexa Fluor 488 Antibody (1:500 for IF,  
701 Invitrogen; A-11008), goat anti-mouse Alexa Fluor 594 Antibody (1:500 for IF, Invitrogen; A-  
702 11005), HRP-conjugated Affinipure Goat Anti-Rabbit Antibody (1:10000 for WB, Proteintech,  
703 SA00001-4), HRP-conjugated Affinipure Goat Anti-Mouse Antibody (1:10000 for WB,  
704 Proteintech, SA00001-1).

705

## 706 **Plasmids**

707 The psiCHECK2-*NIPBL*-3'UTR luciferase reporter plasmid was created by amplifying a 449 bp  
708 fragment of the *NIPBL* 3'UTR from human genomic DNA through PCR and cloning it into the  
709 XhoI and NotI sites of psiCHECK-2 (Promega, Madison, WI, USA). To generate the mutations

---

710 plasmid corresponding miR-187 binding sites, the plasmid of psiCHECK2-*NIPBL*-3'UTR-MUT  
711 was subjected to site-directed mutagenesis through PCR, and the resulting mutations were  
712 verified by DNA sequencing.

713  
714 For the lentiviral vector pLJM1-pri-miR-187, a 586 bp human genomic DNA fragment,  
715 including pri-miR-187, was amplified by PCR and cloned into the NheI and EcoRI sites of  
716 pLJM1- (Addgene, Watertown, MA, USA).

717 The expression plasmids *NIPBL* were constructed by cloning the cDNA of *NIPBL* into pCDH-  
718 4HA.

#### 719 720 **Immunoblot analysis**

721 In Western blot analysis, cells were washed with cold PBS and then lysed in cold Western lysis  
722 buffer (Beyotime, Shanghai, China; p0013) with a protease inhibitor cocktail (Roche, Basel,  
723 Switzerland, 04693132001). A standard procedure was used for the immunoblot analysis of  
724 total protein from the whole-cell lysate. *GAPDH* or *H3* was used as an internal control to  
725 normalize the protein loading.

#### 726 727 **Luciferase reporter assay**

728 The luciferase reporter plasmids psi-CHECK2-*NIPBL*-3'UTR or mutants were cotransfected  
729 into HEK293T or EA.hy926 cells seeded in 24-well plates along with 100 nM miR-187 mimic  
730 or miR-NC mimic and Lipofectamine 3000. After 36 hours, the cells were washed three times  
731 with cold PBS and lysed in a passive lysis buffer. Luciferase activity was measured using a



---

Dual-Luciferase Assay System (Promega; E1960) on a GloMax-Multi Detection System plate reader (Promega).

#### **miRNA pulldown assay**

In the miRNA pulldown experiment, biotin-labeled double-stranded miR-187 mimic or miR-NC mimic was transfected into hESC-ECs with Lipofectamine RNAiMAX Transfection Reagent. After 24 hours, the cells were harvested, and RNP complexes with the target mRNAs were pulled down by Dynabeads M-280 Streptavidin (Invitrogen; 11205D). To determine the binding specificity of miR-187 to *NIPBL* mRNA, RT-qPCR analyzed the target mRNAs, and the enrichment of the target mRNAs was calculated as follows: (*NIPBL* mRNA pulled down by miR-187/*NIPBL* mRNA pulled down by miR-NC mimic)/(Biotin-miR-187 input/Biotin-miR-NC mimic input). The experiments were performed at least three times, with three replicates for each set.

#### **Formation and culture of HFOs**

The protocol of HFO formation was modified from the previous publications (34). The hESCs were maintained on Matrigel Matrix (1:200, Corning, 354277) in mTeSR1 medium plus. For HFO formation, hESCs were detached, and  $3 \times 10^4$  cells per well were seeded in a U-shaped ultralow-attachment 96-well plate (NEST, 701101) in mTeSR1 medium plus. The plate was incubated to allow one aggregate per well to form overnight. On day 0, each aggregate was embedded in a Matrigel (Corning, 356231) droplet. Differentiation was initiated on day 0 by replacing the medium with RPMI1640 medium containing B27 supplement without insulin

---

(RB-) and supplemented with 7.5  $\mu$ M CHIR-99021. After 24 hours, the medium was exchanged by RB-, and on d1, RB- supplemented with 5  $\mu$ M IWR-1 (Sigma-Aldrich; I0161) was added for 48 hours and exchanged by RB- on day 3. From day 7 onwards, aggregates were cultivated in RPMI1640 medium containing B27 supplement with insulin (Gibco; 17504044) (RB+). Differentiation was completed on day 7. HFOs were analyzed between day 8 and day 10, and took pictures of the whole HFOs were using a Castor X1 High-throughput cell analyzer (Countstar, Shanghai, China). Doxorubicin (500 nM) was administered during days -1 to 10 of HFOs.

#### **Migration assay**

The effect of miR-187 and *NIPBL* on hESC-ECs migration was assessed using wound healing assays. A total of  $1 \times 10^5$  cells were seeded in 6-well plates and allowed to culture for 24 hours. After 48 hours, transfection was performed using Lipofectamine 3000 with miR-187 mimic only, co-expressed miR-187/NIPBL, or scramble control. The cells were cultured until they reached confluence. Subsequently, scratches were created on the cell layers using a 1 mL pipette tip. The recovered area of the scratches was evaluated after 24 hours using an inverted light microscope.

#### **Tube formation assay**

hESC-ECs were seeded at  $1 \times 10^4$  cells/cm<sup>2</sup> density on a 24-well plate coated with 250  $\mu$ l of Matrigel (Corning, 356231) in EGM-2 medium. The plate was then incubated for 24 hours at 37°C in a 5% CO<sub>2</sub> atmosphere. After incubation, the medium was removed, and the plates

---

were washed with PBS. The formation of capillary-like structures was observed using an inverted light microscope. Tube formation was quantified using ImageJ 1.52a software (Wayne Rasband, National Institute of Health, USA) and the Angiogenesis Analyzer plugin (Gilles Carpentier, Universite Paris Est Creteil Val de Marne, France).

## **Zebrafish studies**

In a zebrafish study, microinjection of exogenous dre-miR-187-3p mimic or negative control (all at 20 pM) into fertilized cmlc2-DsRed (labeling CM nucleus) or cmlc2-EGFP (labeling CM membrane) zebrafish embryos. Zebrafish cardiac morphology was measured with confocal microscopy 72 hours post fertilization (hpf).

## **Statistical Analyses**

Data are presented as mean values with corresponding standard deviations (SD). Tukey's multiple comparisons test was used for Figures 3A, 3C-H, 3M-N, 4I-N, 5C-F, S3C, S3E-F, S3L-N, S5A, S5C-F, S6E, S8C-F, S10A, S10C-D, and S13D. Others statistical significance of the differences between groups was determined using two-sided Student's t-tests, and p-values are reported. Differences in phenotype frequencies (Figure S3B) between the KI/KI, KI/+, and +/+ mice were evaluated using Pearson's  $\chi^2$ -test. The significance level is denoted by asterisks, with \* indicating  $p < 0.05$ , \*\* indicating  $p < 0.01$ , \*\*\* indicating  $p < 0.001$ , and \*\*\*\* indicating  $p < 0.0001$ .

## **Study approval**

---

All procedures to use mice for the current study were approved by the Institute of Developmental Biology and Molecular Medicine of the Fudan University. All procedures to use human specimens for the current study were approved by the Institutional Review Board of the Fudan University.

### **Data availability**

All data are available from the corresponding author upon reasonable request. The datasets generated during this study have been uploaded to the Gene Expression Omnibus database under the following accession codes: GSE275849, GSE275950, and GSE275951 for RNA-seq; GSE276221 and GSE276222 for ATAC-seq; GSE275850 for CUT&TAG-seq. Supporting data values are available.

### **Funding**

This work was supported by grants from the National Key R&D Program of China (2021YFC2701101, H.W. and 2021YFC2701103 to J.S.), the National Natural Science Foundation of China (81930036 and 82150008, H.W.), Basic Science Center Program (32488101, H.W.) and China Postdoctoral Science Foundation (2023T160113 to C.L.)

### **Acknowledgments**

We thank the patient's family for their valuable collaboration in this study. We want to acknowledge Dr. Hongtao Yu for providing the *NIPBL* plasmid. We are also grateful to Drs.

---

Duan Ma, Xiaotian Li, and Jizi Zhou for sharing the original RNA profile data collected from children with CHD. We also thank Dr. Bing Zhao for his assistance in the HFO experiment.

#### **Author contributions**

CL, ZT, JS, and HW designed the study. CL, ZT, HL, CP and YQ conducted experiments. CL and ZT performed data mining, RNA-seq profiling, sequencing analysis, cell and mouse experiments. CL and ZT for their assistance with HFOs and hESC-ECs culture and differentiation systems. CL and XY optimized the tissue dissociation protocol and collected TOF samples. CL, ZT and HW interpreted the results, and CL, ZT, HL, YQ, JS and HW wrote the manuscript. HW and JS supervised the project and provided financial support.

#### **Conflict of interest**

The authors have declared that no conflict of interest exists.

#### **Ethical approval**

All experiments involving human tissue samples were performed following the Declaration of Helsinki. All experiments involving human tissue samples and animals were conducted with approval from the Medical Ethics Committee at the Obstetrics & Gynecology Hospital of Fudan University.

#### **Abbreviation**

miR-187: miR-187-3p; +/-: WT; KI/+ : heterozygous Rosa26- *Tek*-mir-187 knock-in, KI/KI:

---

841 homozygous *Rosa26-Tek-mir-18* knock-in; RV: right ventricle; LV: left ventricle; IVS:  
842 interventricular septum; EC: endothelial cell; CM: cardiomyocyte; hESCs: human embryonic  
843 stem cells; BW: body weight; HW: heart weight; Rel.: relative; Luc.: luciferase; Ctrl: control.  
844 HFOs: human heart-forming organoids.  
845

## References

1. Hill MC, Kadow ZA, Long H, Morikawa Y, Martin TJ, Birks EJ, et al. Integrated multi-omic characterization of congenital heart disease. *Nature*. 2022;608(7921):181-91.
2. Turner ME, Bouhout I, Petit CJ, and Kalfa D. Transcatheter Closure of Atrial and Ventricular Septal Defects: JACC Focus Seminar. *Journal of the American College of Cardiology*. 2022;79(22):2247-58.
3. Minette MS, and Sahn DJ. Ventricular septal defects. *Circulation*. 2006;114(20):2190-7.
4. Kuo CF, Lin YS, Chang SH, Chou IJ, Luo SF, See LC, et al. Familial Aggregation and Heritability of Congenital Heart Defects. *Circulation journal : official journal of the Japanese Circulation Society*. 2017;82(1):232-8.
5. Greenway SC, Pereira AC, Lin JC, DePalma SR, Israel SJ, Mesquita SM, et al. De novo copy number variants identify new genes and loci in isolated sporadic tetralogy of Fallot. *Nature genetics*. 2009;41(8):931-5.
6. Morton SU, Quiat D, Seidman JG, and Seidman CE. Genomic frontiers in congenital heart disease. *Nature reviews Cardiology*. 2022;19(1):26-42.
7. Fahed AC, Gelb BD, Seidman JG, and Seidman CE. Genetics of congenital heart disease: the glass half empty. *Circulation research*. 2013;112(4):707-20.
8. Chen J, and Wang DZ. microRNAs in cardiovascular development. *Journal of molecular and cellular cardiology*. 2012;52(5):949-57.
9. Porrello ER. microRNAs in cardiac development and regeneration. *Clin Sci (Lond)*. 2013;125(4):151-66.
10. Bischoff J. Endothelial-to-Mesenchymal Transition. *Circulation research*. 2019;124(8):1163-5.
11. Nagy O, Baráth S, and Ujfalusi A. The role of microRNAs in congenital heart disease. *Ejifcc*. 2019;30(2):165-78.
12. Porrello ER, Johnson BA, Aurora AB, Simpson E, Nam YJ, Matkovich SJ, et al. MiR-15 family regulates postnatal mitotic arrest of cardiomyocytes. *Circulation research*. 2011;109(6):670-9.
13. Zhao Y, Ransom JF, Li A, Vedantham V, von Drehle M, Muth AN, et al. Dysregulation of cardiogenesis, cardiac conduction, and cell cycle in mice lacking miRNA-1-2. *Cell*. 2007;129(2):303-17.
14. Boettger T, and Braun T. A new level of complexity: the role of microRNAs in cardiovascular development. *Circulation research*. 2012;110(7):1000-13.
15. Pinto AR, Illykh A, Ivey MJ, Kuwabara JT, D'Antoni ML, Debuque R, et al. Revisiting Cardiac Cellular Composition. *Circulation research*. 2016;118(3):400-9.
16. Karlsson M, Zhang C, Méar L, Zhong W, Digre A, Katona B, et al. A single-cell type transcriptomics map of human tissues. *Science advances*. 2021;7(31).
17. Hofmann JJ, Briot A, Enciso J, Zovein AC, Ren S, Zhang ZW, et al. Endothelial deletion of murine Jag1 leads to valve calcification and congenital heart defects associated with Alagille syndrome. *Development*. 2012;139(23):4449-60.
18. Ameen M, Sundaram L, Shen M, Banerjee A, Kundu S, Nair S, et al. Integrative single-cell analysis of cardiogenesis identifies developmental trajectories and non-coding mutations in congenital heart disease. *Cell*. 2022;185(26):4937-53.e23.

- 
- 889 19. Muñoz S, Minamino M, Casas-Delucchi CS, Patel H, and Uhlmann F. A Role for Chromatin  
890 Remodeling in Cohesin Loading onto Chromosomes. *Molecular cell*. 2019;74(4):664-  
891 73.e5.
  - 892 20. Merckenschlager M, and Nora EP. CTCF and Cohesin in Genome Folding and  
893 Transcriptional Gene Regulation. *Annual review of genomics and human genetics*.  
894 2016;17:17-43.
  - 895 21. Emerson DJ, Zhao PA, Cook AL, Barnett RJ, Klein KN, Saulebekova D, et al. Cohesin-  
896 mediated loop anchors confine the locations of human replication origins. *Nature*.  
897 2022;606(7915):812-9.
  - 898 22. Yatskevich S, Rhodes J, and Nasmyth K. Organization of Chromosomal DNA by SMC  
899 Complexes. *Annual review of genetics*. 2019;53:445-82.
  - 900 23. Bernardi G. The formation of chromatin domains involves a primary step based on the 3-  
901 D structure of DNA. *Scientific reports*. 2018;8(1):17821.
  - 902 24. Krantz ID, McCallum J, DeScipio C, Kaur M, Gillis LA, Yaeger D, et al. Cornelia de Lange  
903 syndrome is caused by mutations in NIPBL, the human homolog of *Drosophila*  
904 *melanogaster* Nipped-B. *Nature genetics*. 2004;36(6):631-5.
  - 905 25. Kline AD, Moss JF, Selicorni A, Bisgaard AM, Deardorff MA, Gillett PM, et al. Diagnosis and  
906 management of Cornelia de Lange syndrome: first international consensus statement.  
907 *Nature reviews Genetics*. 2018;19(10):649-66.
  - 908 26. Chatfield KC, Schrier SA, Li J, Clark D, Kaur M, Kline AD, et al. Congenital heart disease in  
909 Cornelia de Lange syndrome: phenotype and genotype analysis. *American journal of*  
910 *medical genetics Part A*. 2012;158a(10):2499-505.
  - 911 27. Selicorni A, Colli AM, Passarini A, Milani D, Cereda A, Cerutti M, et al. Analysis of congenital  
912 heart defects in 87 consecutive patients with Brachmann-de Lange syndrome. *American*  
913 *journal of medical genetics Part A*. 2009;149a(6):1268-72.
  - 914 28. Boyle MI, Jespersgaard C, Brøndum-Nielsen K, Bisgaard AM, and Tümer Z. Cornelia de  
915 Lange syndrome. *Clinical genetics*. 2015;88(1):1-12.
  - 916 29. Santos R, Kawauchi S, Jacobs RE, Lopez-Burks ME, Choi H, Wikenheiser J, et al. Conditional  
917 Creation and Rescue of Nipbl-Deficiency in Mice Reveals Multiple Determinants of Risk  
918 for Congenital Heart Defects. *PLoS biology*. 2016;14(9):e2000197.
  - 919 30. Hamad S, Derichsweiler D, Gaspar JA, Brockmeier K, Hescheler J, Sachinidis A, et al. High-  
920 efficient serum-free differentiation of endothelial cells from human iPS cells. *Stem cell*  
921 *research & therapy*. 2022;13(1):251.
  - 922 31. Duan F, Li H, and Lu H. In vivo and molecular docking studies of the pathological  
923 mechanism underlying adriamycin cardiotoxicity. *Ecotoxicol Environ Saf*. 2023;256:114778.
  - 924 32. Berry GJ, Rizeq MN, Weiss LM, and Billingham ME. Graft coronary disease in pediatric  
925 heart and combined heart-lung transplant recipients: a study of fifteen cases. *J Heart Lung*  
926 *Transplant*. 1993;12(6 Pt 2):S309-19.
  - 927 33. Chaudhari U, Nemade H, Gaspar JA, Hescheler J, Hengstler JG, and Sachinidis A.  
928 MicroRNAs as early toxicity signatures of doxorubicin in human-induced pluripotent stem  
929 cell-derived cardiomyocytes. *Arch Toxicol*. 2016;90(12):3087-98.
  - 930 34. Drakhlis L, Biswanath S, Farr CM, Lupanow V, Teske J, Ritzenhoff K, et al. Human heart-  
931 forming organoids recapitulate early heart and foregut development. *Nature*  
932 *biotechnology*. 2021;39(6):737-46.



35. Lewis-Israeli YR, Wasserman AH, Gabalski MA, Volmert BD, Ming Y, Ball KA, et al. Self-assembling human heart organoids for the modeling of cardiac development and congenital heart disease. *Nat Commun.* 2021;12(1):5142.
36. Mulrane L, Madden SF, Brennan DJ, Gremel G, McGee SF, McNally S, et al. miR-187 is an independent prognostic factor in breast cancer and confers increased invasive potential in vitro. *Clinical cancer research : an official journal of the American Association for Cancer Research.* 2012;18(24):6702-13.
37. Cai Y, Ruan J, Yao X, Zhao L, and Wang B. MicroRNA-187 modulates epithelial-mesenchymal transition by targeting PTRF in non-small cell lung cancer. *Oncology reports.* 2017;37(5):2787-94.
38. Zhang QL, Wang W, Li J, Tian SY, and Zhang TZ. Decreased miR-187 induces retinal ganglion cell apoptosis through upregulating SMAD7 in glaucoma. *Biomedicine & pharmacotherapy = Biomedecine & pharmacotherapie.* 2015;75:19-25.
39. Gao D, Zhu B, Cao X, Zhang M, and Wang X. Roles of NIPBL in maintenance of genome stability. *Seminars in cell & developmental biology.* 2019;90:181-6.
40. Li Y, Lui KO, and Zhou B. Reassessing endothelial-to-mesenchymal transition in cardiovascular diseases. *Nature reviews Cardiology.* 2018;15(8):445-56.
41. Locke JM, da Silva Xavier G, Dawe HR, Rutter GA, and Harries LW. Increased expression of miR-187 in human islets from individuals with type 2 diabetes is associated with reduced glucose-stimulated insulin secretion. *Diabetologia.* 2014;57(1):122-8.
42. Fan L, Yang K, Yu R, Hui H, and Wu W. circ-lqsec1 induces bone marrow-derived mesenchymal stem cell (BMSC) osteogenic differentiation through the miR-187-3p/Satb2 signaling pathway. *Arthritis research & therapy.* 2022;24(1):273.
43. Bassat E, Mutlak YE, Genzelinakh A, Shadrin IY, Baruch Umansky K, Yifa O, et al. The extracellular matrix protein agrin promotes heart regeneration in mice. *Nature.* 2017;547(7662):179-84.
44. Li C, Li H, Yao X, Liu D, Wang Y, Huang X, et al. Master microRNA-222 regulates cardiac microRNA maturation and triggers Tetralogy of Fallot. *Signal transduction and targeted therapy.* 2022;7(1):165.
45. Nolen LD, Boyle S, Ansari M, Pritchard E, and Bickmore WA. Regional chromatin decompaction in Cornelia de Lange syndrome associated with NIPBL disruption can be uncoupled from cohesin and CTCF. *Human molecular genetics.* 2013;22(20):4180-93.
46. D'Alessandro LC, Al Turki S, Manickaraj AK, Manase D, Mulder BJ, Bergin L, et al. Exome sequencing identifies rare variants in multiple genes in atrioventricular septal defect. *Genetics in medicine : official journal of the American College of Medical Genetics.* 2016;18(2):189-98.
47. Braunholz D, Hullings M, Gil-Rodriguez MC, Fincher CT, Mallozzi MB, Loy E, et al. Isolated NIBPL missense mutations that cause Cornelia de Lange syndrome alter MAU2 interaction. *European journal of human genetics : EJHG.* 2012;20(3):271-6.
48. Chen W, and Li S. Circulating microRNA as a Novel Biomarker for Pulmonary Arterial Hypertension Due to Congenital Heart Disease. *Pediatric cardiology.* 2017;38(1):86-94.
49. Yost KE, Carter AC, Xu J, Litzenburger U, and Chang HY. ATAC Primer Tool for targeted analysis of accessible chromatin. *Nature methods.* 2018;15(5):304-5.

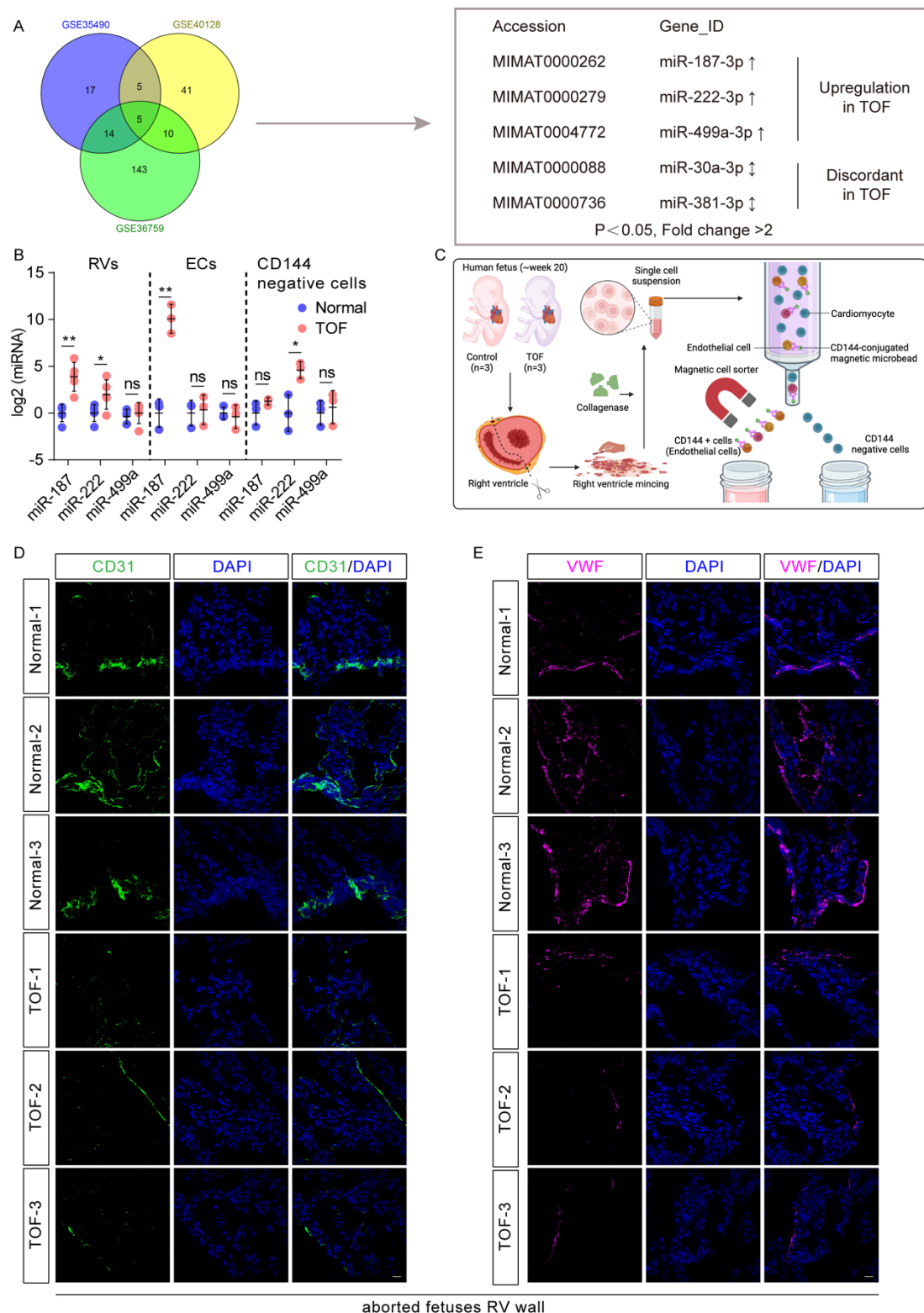


**Figure 1. Upregulation of miR-187 expression in the hearts of fetuses with TOF. (A)** Schematic illustration of the screening process for differentially expressed microRNAs (fold change  $> 2$ ,  $P < 0.05$ ) using three independent datasets (GSE35490, GSE36759 and GSE40128). **(B)** RT-qPCR analysis of miR-187, miR-222 and miR-499a levels in the RVs, ECs and CMs of aborted fetuses with TOF (for RVs  $n=5$ , for ECs and CMs  $n=3$ ) and normal controls (for RVs  $n=5$ , for ECs and CMs  $n=3$ ). U6 was used as an internal control. **(C)** Schematic diagram

of the isolation of endothelial cells from human hearts. **(D, E)** Representative immunofluorescence staining of endothelial marker CD31 (green, **D**) and VWF (violet, **E**) in heart sections from right ventricle wall tissues from  $\approx 20$  weeks aborted fetuses with TOF ( $n=3$ ) and normal controls ( $n=3$ ). DAPI was used for nuclear staining (blue). The scale bars in **(C)** and **(D)** are 20  $\mu\text{m}$ . Data are shown as means  $\pm$  SD. ns  $P > 0.05$ ,  $*P < 0.05$ ,  $**P < 0.01$ . Significance was determined by 1-way ANOVA (**B**).

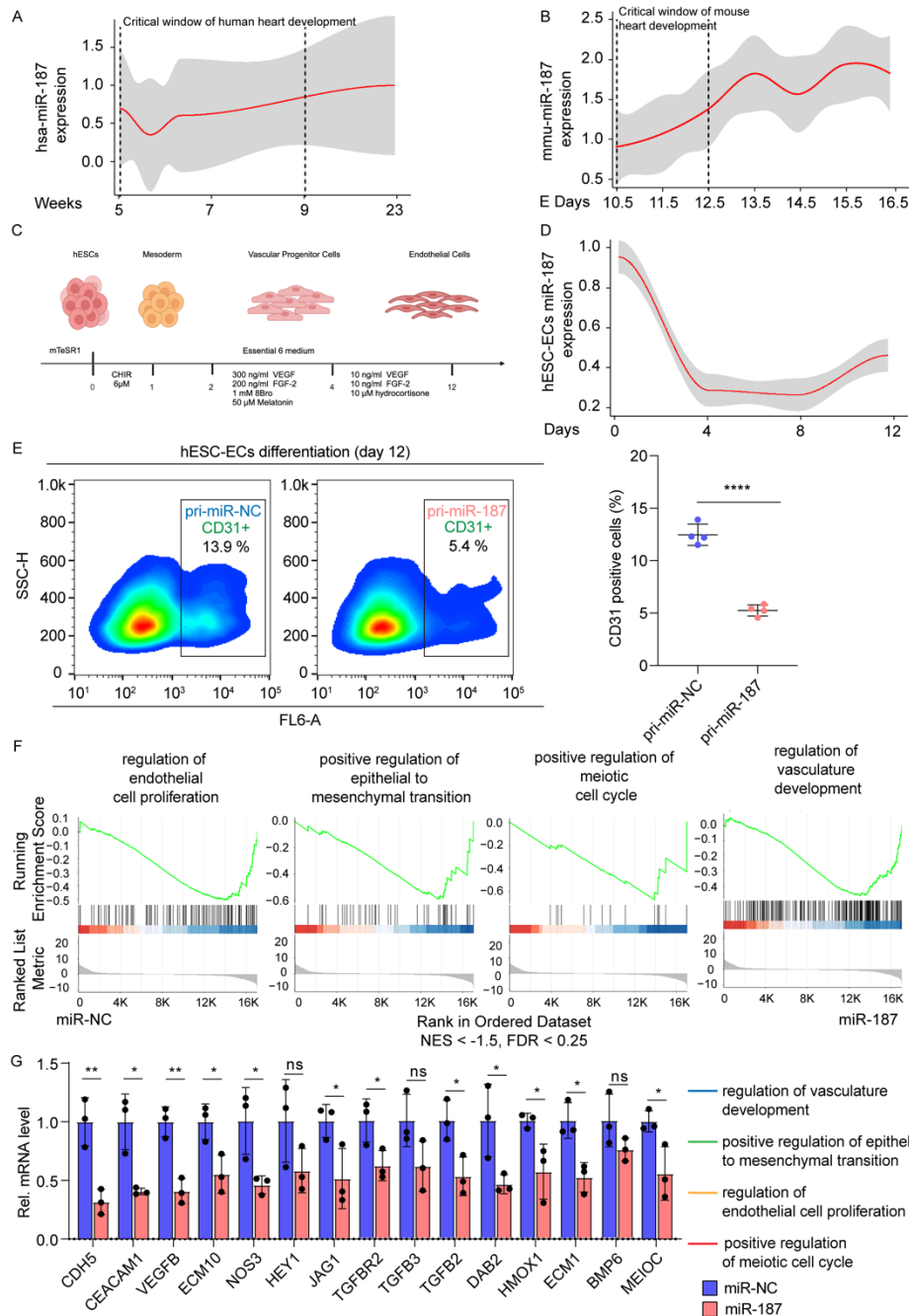


**Figure 2. High miR-187 expression levels impair endothelial development. (A, B, D)** Temporal analysis of miR-187 expression during normal human heart development by microarray analyses **(A)** and mouse heart development using the GSE105834, GSE82960, GSE105910, GSE82604, GSE82822, GSE82942, and GSE101175 datasets **(B)** and differentiation of hESCs into ECs by RT-qPCR ( $n=4$ ) **(D)**. **(C)** Schematic of protocol for differentiation from

---

hESCs to ECs. **(E)** FACS analysis and quantification of CD31 positive cells in hESC-ECs infection with pri-miR-187 or scramble control by lentivirus (n=4). **(F)** Representative GSEA results for regulation of endothelial cell proliferation (GO:0001936), positive regulation of epithelial to mesenchymal transition (GO:0010718), positive regulation of meiotic cell cycle (GO:0051446) and regulation of vasculature development (GO:1901342) gene sets. **(G)** RT-qPCR verification of representative genes of GO:0001936, GO:0010718, GO:0051446 and GO:1901342 gene sets (n=3). U6 or GAPDH was used as an internal control. Data are shown as means  $\pm$  SD. ns  $P > 0.05$ ,  $*P < 0.05$ ,  $**P < 0.01$ ,  $****P < 0.0001$ . Significance was determined by 1-way ANOVA (G) and 2-tailed t test (E).

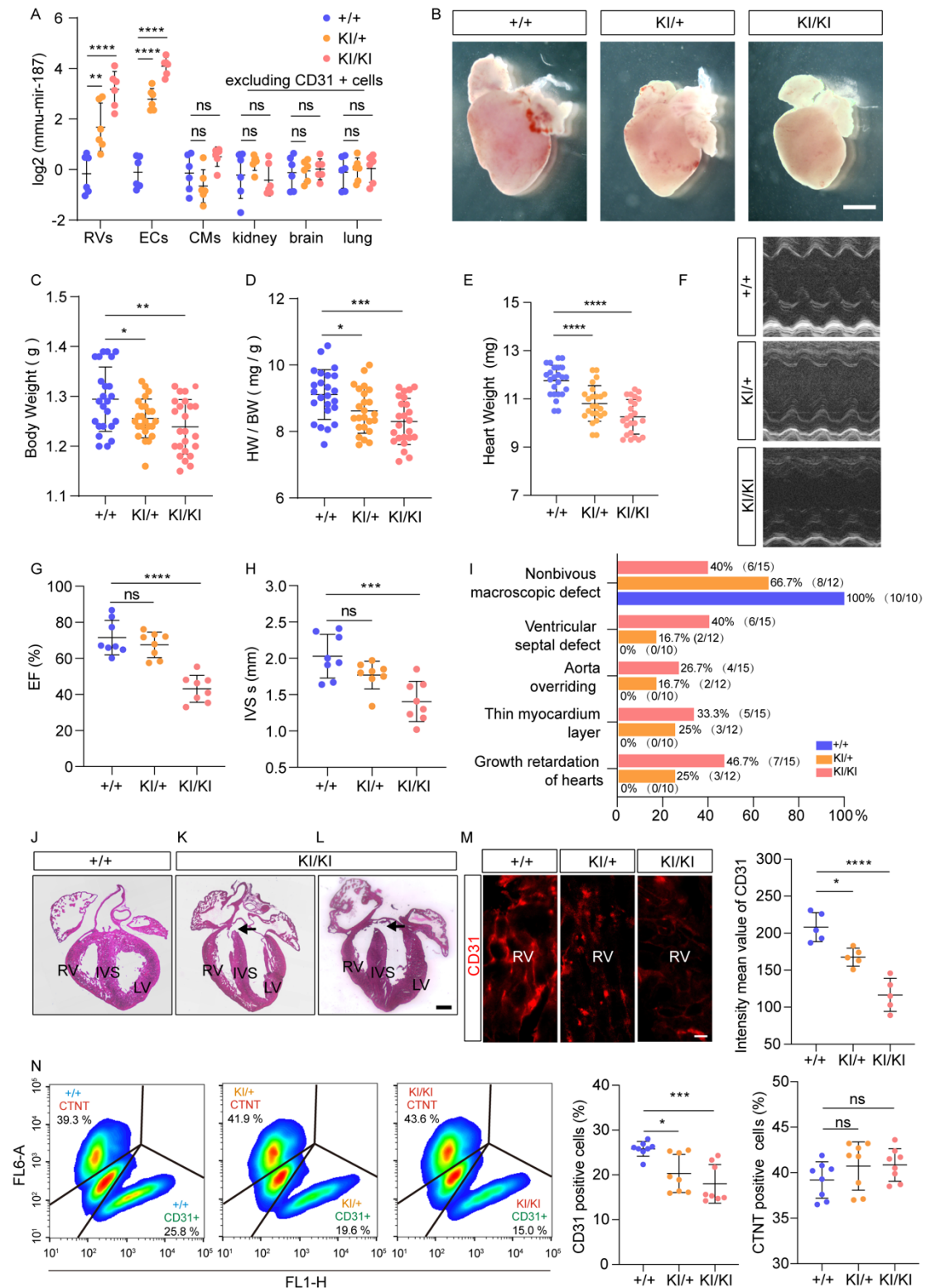


**Figure 3. Endothelial-specific expression of exogenous miR-187 drives congenital heart disease.** (A) RT-qPCR analysis of mmu-mir-187 levels in the hearts, ECs, CMs and other tissues excluding CD31 positive cells (kidneys, brains, and lungs) of P0 neonatal mice with the indicated genotypes (n=6). (B) Stereoscopic images of whole hearts from homozygous, heterozygous mir-187 KI and control mice at P0. (C-E) Body weight (C), heart weight / body weight ratio (D) and heart weight (E) of P0.5 neonatal homozygous mir-187-knock-in (KI)

---

and control mice (n=24). **(F-H)** Echocardiographic assessment of representative M-mode images of the left ventricle **(F)**, ejection fraction **(G)** and systolic intraventricular septum **(H)** in control mice and miR-187 KI mice (n=8). IVS s, systolic intraventricular septum; EF, ejection fraction. **(I)** Quantification of cardiac defect number according to stereoscopic images and H&E-stained sections of whole hearts of control mice and homozygous mir-187 KI mice. **(J-L)** H&E-stained heart sections from homozygous mir-187 KI and control mice, displaying human CHD-like phenotypes, such as **(J)** the control heart shows a normal septum; A mir-187 KI littermate of the animal in **(K, L)** shows VSD (arrow, **K**) and aorta overriding (arrow, **L**) at P0.5. **(M)** Quantification of the intensity mean value of CD31 (red) per field of view (n=5). **(N)** FACS analysis and quantification of CTNT and CD31 positive cells from homozygous, heterozygous mir-187 KI and control mice at P0.5 (n=8). The scale bars in **(B)**, **(J-L)** and **(M)** are 1000  $\mu$ m, 200  $\mu$ m and 5  $\mu$ m, respectively. Data are shown as means  $\pm$  SD. ns  $P > 0.05$ ,  $*P < 0.05$ ,  $**P < 0.01$ ,  $***P < 0.0001$ . Significance was determined by 1-way ANOVA (A, C-E, G, H, M and N) and Pearson's  $\chi^2$ -test (I).

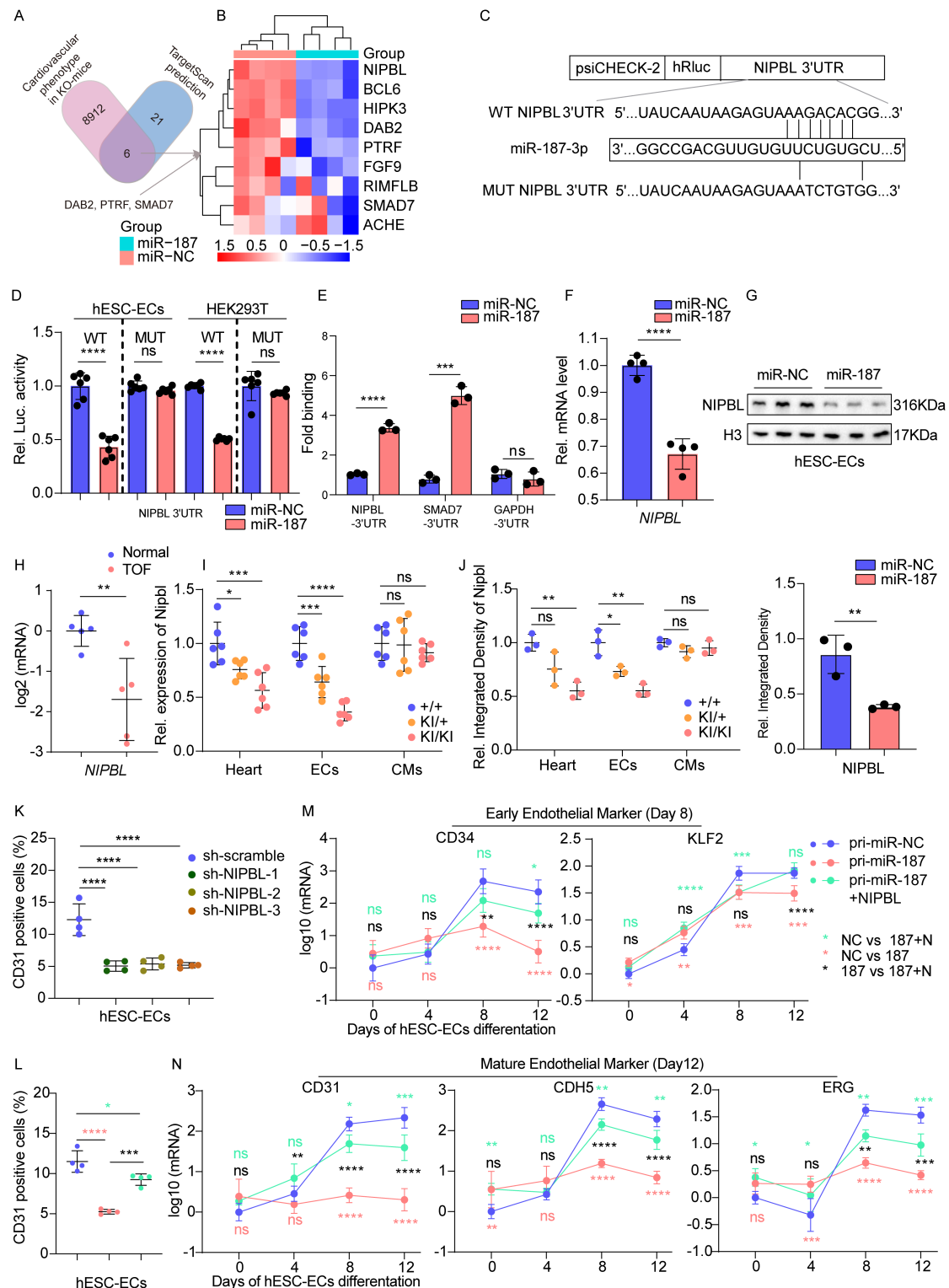


**Figure 4. MiR-187 targets NIPBL and disturbs endothelial development.** (A) Schematic illustration of the screening approach for target genes of miR-187 using TargetScan prediction, MGI database, and RT-qPCR verification. (B) Cluster analysis of RT-qPCR results showing the expression levels of candidate target genes of miR-187 in hESC-ECs transfected with miR-187 mimic. (C) Schematic illustration of luciferase reporters containing WT and mutant miR-187 binding sites in the NIPBL 3'UTR. (D) Luciferase assays of hESC-ECs or HEK293T cells co-transfected with miR-187 or scramble control and luciferase reporter

---

1034 plasmids containing WT or mutant NIPBL 3'UTR. **(E)** The human NIPBL 3'UTR pulled down by  
1035 biotin-miR-187 or biotin-scramble control was quantified by RT-qPCR in hESC-ECs. SMAD7-  
1036 3'UTR and GAPDH-3'UTR serve as positive and negative controls, respectively. **(F, G)** RT-  
1037 qPCR and western blotting were used to analyze the mRNA **(F)** and protein **(G, up)** levels of  
1038 NIPBL in hESC-ECs transfected with miR-187 or scramble control, with grayscale analysis  
1039 employed to quantify the NIPBL protein **(G, down)**. **(H)** RT-qPCR analysis of the mRNA levels  
1040 of NIPBL in the RVs of aborted fetuses with TOF and control fetuses (n=5). **(I, J)** The mRNA **(I)**  
1041 and protein level **(J)** of Nipbl in whole hearts, cardiac endothelial cells and cardiomyocytes of  
1042 P0 neonatal mice of the indicated genotypes (n=6). **(K, L)** FACS quantification of CD31  
1043 positive cells in hESC-ECs infection with sh-NIPBL-1, 2, 3, sh-scramble **(K)** pri-miR-187, pri-  
1044 miR-187+NIPBL or scramble control by lentivirus (n=4) **(L)**. **(M, N)** RT-qPCR analyses of  
1045 expression levels of various markers for early endothelial **(M)** and mature endothelial cells **(N)**  
1046 during differentiation from hESCs to endothelial cells (n=4). GAPDH or H3 was used as an  
1047 internal control. Data are shown as means  $\pm$  SD. ns  $P > 0.05$ , \* $P < 0.05$ , \*\* $P < 0.01$ , \*\*\*\* $P$   
1048  $< 0.0001$ . Significance was determined by 1-way ANOVA (D, E, I-L), 2-way ANOVA (M and  
1049 N) and 2-tailed t test (F-H).



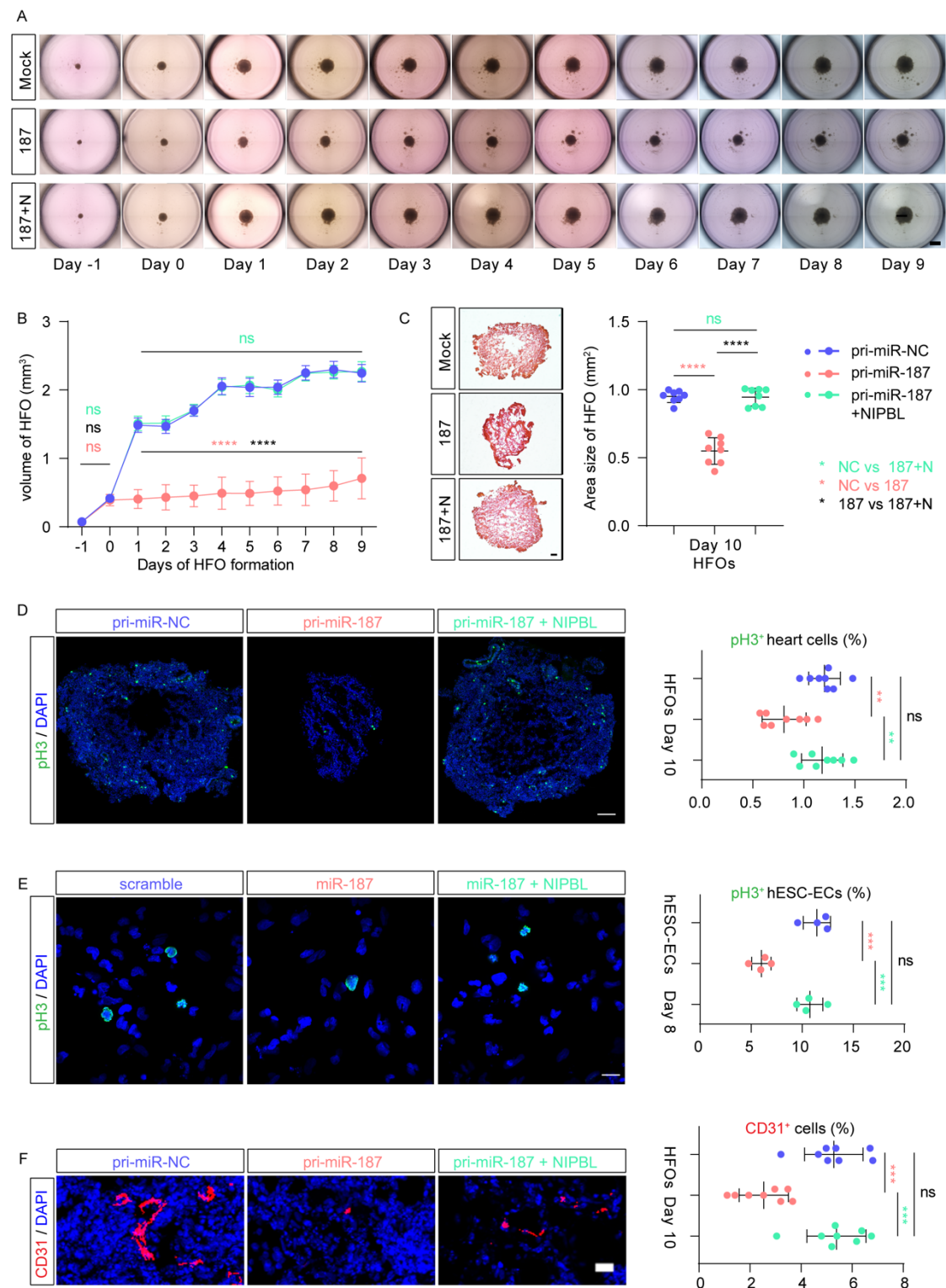
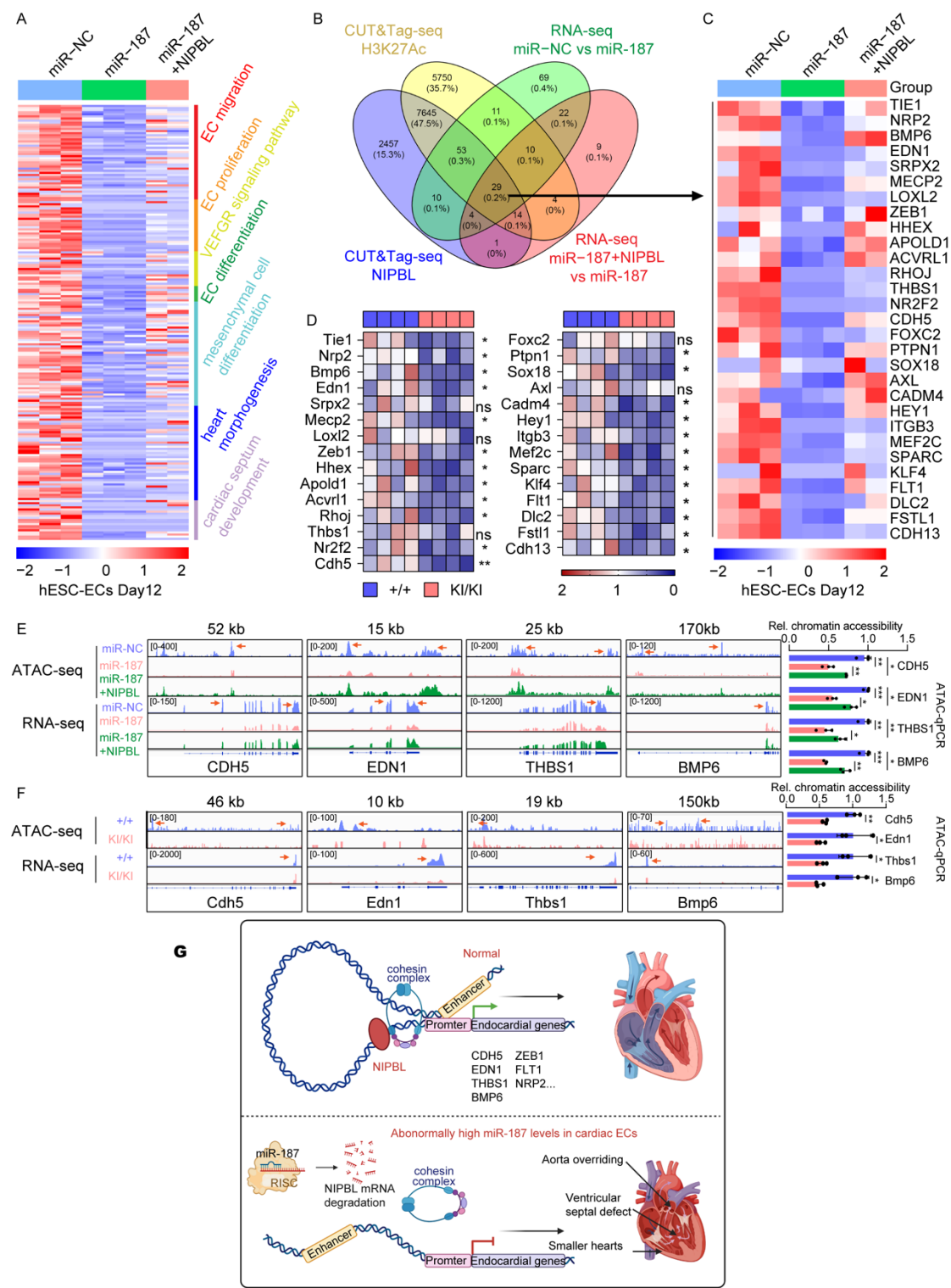


**Figure 5. NIPBL rescues delaying HFO formation induced by miR-187.** (A) The figure shows the development of HFOs from day -1 until day 9 of mock, miR-187 and miR-187/NIPBL differentiation. (B) Quantification of volume of HFOs (n=32) from day -1 until day 9 of mock, miR-187 and miR-187/NIPBL differentiation. (C) H&E staining (left) and quantification (n=8) (right) of area for mock, miR-187 and miR-187/NIPBL HFOs at day 10. (D) Immunostainings for pH3 (green, left) and quantification (n=8) (right) show the number of mitotic mock, miR-187 and miR-187/NIPBL HFO cells at day 10. (E) Immunostainings for

pH3 (green, left) and quantification (n=4) (right) show the number of mitotic mock, miR-187  
 and miR-187/NIPBL hESC-ECs at day 8. **(F)** Representative immunofluorescence (red, left)  
 and quantification (n=8) (right) staining of the endothelial cell marker CD31 in mock, miR-  
 187 and miR-187/NIPBL HFO cells at day 10. DAPI was used for nuclear staining (blue). The  
 scale bars in **(A)**, **(C, D)** and **(E, F)** are 1 mm, 100  $\mu$ m and 20  $\mu$ m, respectively. Data are shown  
 as means  $\pm$  SD. ns  $P > 0.05$ ,  $*P < 0.05$ ,  $**P < 0.01$ ,  $****P < 0.0001$ . Significance was  
 determined by 1-way ANOVA (C-F) and 2-way ANOVA (B).



---

**Figure 6. miR-187 reduces endocardial gene expression and chromatin accessibility and inhibits endothelial cells migration and tube formation. (A)** Heat map of RNA-seq analyses of core 208 genes expression levels of gene ontology (GO) terms of GSEA, involved in endothelial cell migration, proliferation, differentiation, vascular endothelial growth factor signaling pathway, mesenchymal cell differentiation, heart morphogenesis and cardiac septum development for miR-NC-hESC-ECs, miR-187-hESC-ECs and miR-187/NIPBL-hESC-ECs. **(B)** Schematic illustration of the screening approach for downstream genes of miR-187/NIPBL axis using NIPBL, H3K27Ac CUT&TAG-seq and miR-NC-hESC-ECs, miR-187-hESC-ECs and miR-187/NIPBL-hESC-ECs RNA-seq. **(C)** Heat map of RNA-seq analyses of 29 screened genes for miR-NC-hESC-ECs, miR-187-hESC-ECs and miR-187/NIPBL-hESC-ECs. **(D)** RT-qPCR analysis of 29 screened genes in endocardial cells of WT and miR-187-KI mice (n=4). Gapdh was used as an internal control. **(E, F)** Genome browser displays representative views of ATAC-seq and RNA-seq signals for the indicated genes (left), while ATAC-qPCR quantification shows the chromatin accessibility of these genes (n=4) (right), comparing hESC-ECs with miR-NC, miR-187, miR-187+NIPBL **(E)**, as well as mice with +/+ and KI/KI genotypes **(F)**. **(G)** Schematic diagram of the role of the miR-187/*NIPBL* axis in the pathogenesis of CHD. Data are shown as means  $\pm$  SD. ns  $P > 0.05$ , \* $P < 0.05$ , \*\* $P < 0.01$ , \*\*\* $P < 0.001$ . Significance was determined by 1-way ANOVA (D-F).

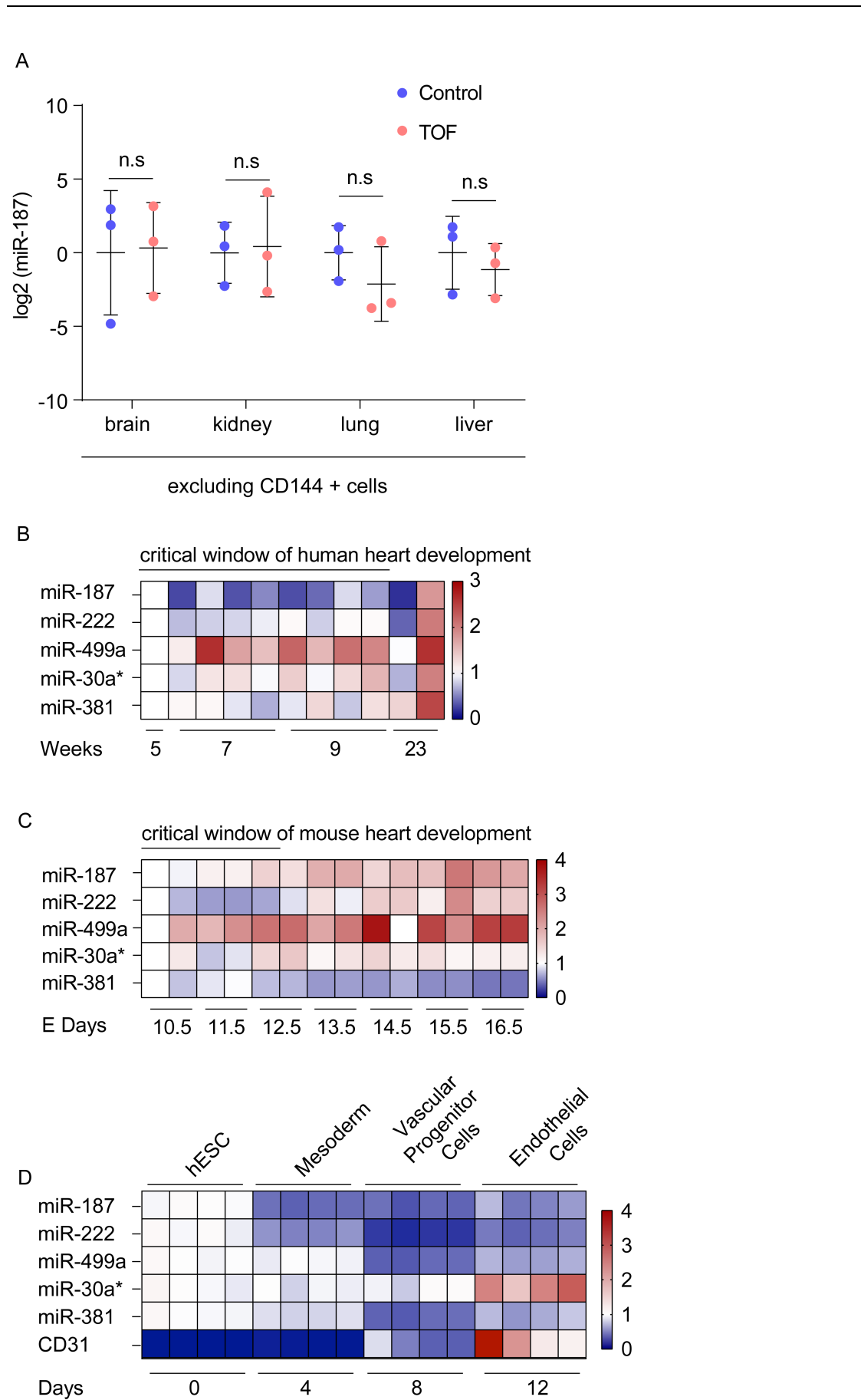
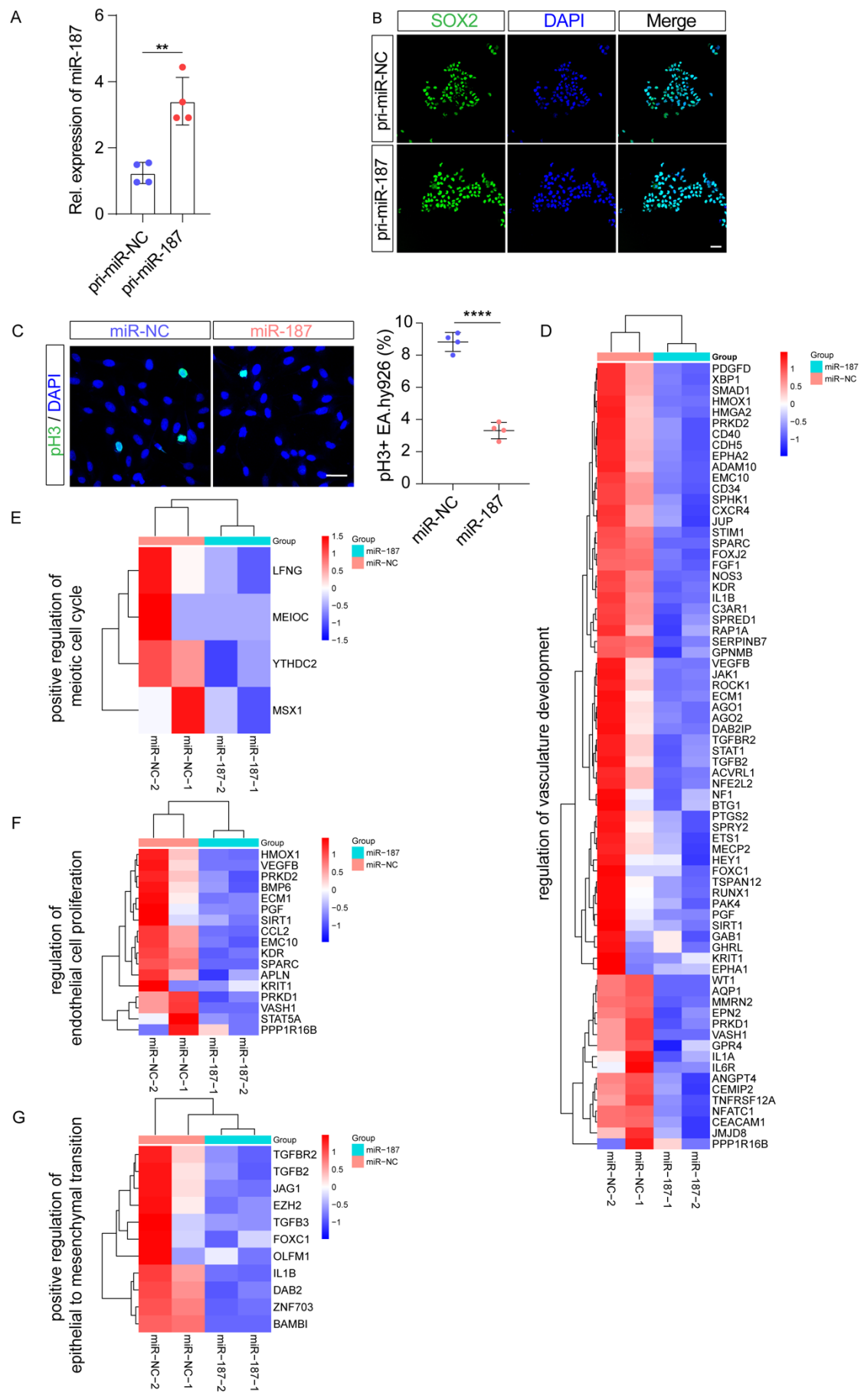


**Figure S1. The expression of miR-187 in other tissues of fetuses with TOF. (A)** RT-qPCR

---

1086 analysis of miR-187 levels in the brains, kidneys, livers, and lungs excluding CD144 positive  
1087 cells (n=3) of aborted fetuses with TOF and normal controls. U6 was used as an internal  
1088 control. Data are shown as means  $\pm$  SD. ns  $P > 0.05$ . **(B-D)** Heatmap representing the levels  
1089 of differentially expressed miRNAs screened by microarray analysis in TOF patients **(B)**, mouse  
1090 heart development using datasets GSE105834, GSE82960, GSE105910, GSE8604, GSE2822,  
1091 GSE892942, and GSE101175 **(C)**, and differentiation of hESCs into ECs by RT-qPCR (n=4) **(D)**.  
1092 Significance was determined by 1-way ANOVA (A).



---

**Figure S2. Construction of stable H9 cell lines expressing miR-187, NIPBL or scramble.**  
(A, B) RT-qPCR analysis of miR-187 level (n=4) (A) and SOX2-immunofluorescence staining for pluripotency marker SOX2 (green) (B) in hESCs infected with lenti-pri-miR-187 or control virus. (C) Immunostainings for pH3 (green, left) and quantification show the number of mitotic mocks in EA.hy926 cells (n=4) (right). (D-G) Heat map showing expression changes of representative genes of regulation of vasculature development (D), positive regulation of meiotic cell cycle (E), regulation of endothelial cell proliferation (F) and positive regulation of epithelial to mesenchymal transition (G) with scramble and downregulation in ectopic expression of miR-187 EA.hy926 cells. The scale bars in (B) and (C) are 50  $\mu$ m and 100  $\mu$ m, respectively. DAPI was used for nuclear staining (blue). Data are shown as means  $\pm$  SD.  $**P < 0.01$ ,  $****P < 0.0001$ . Significance was determined by 2-tailed t test (A and C).



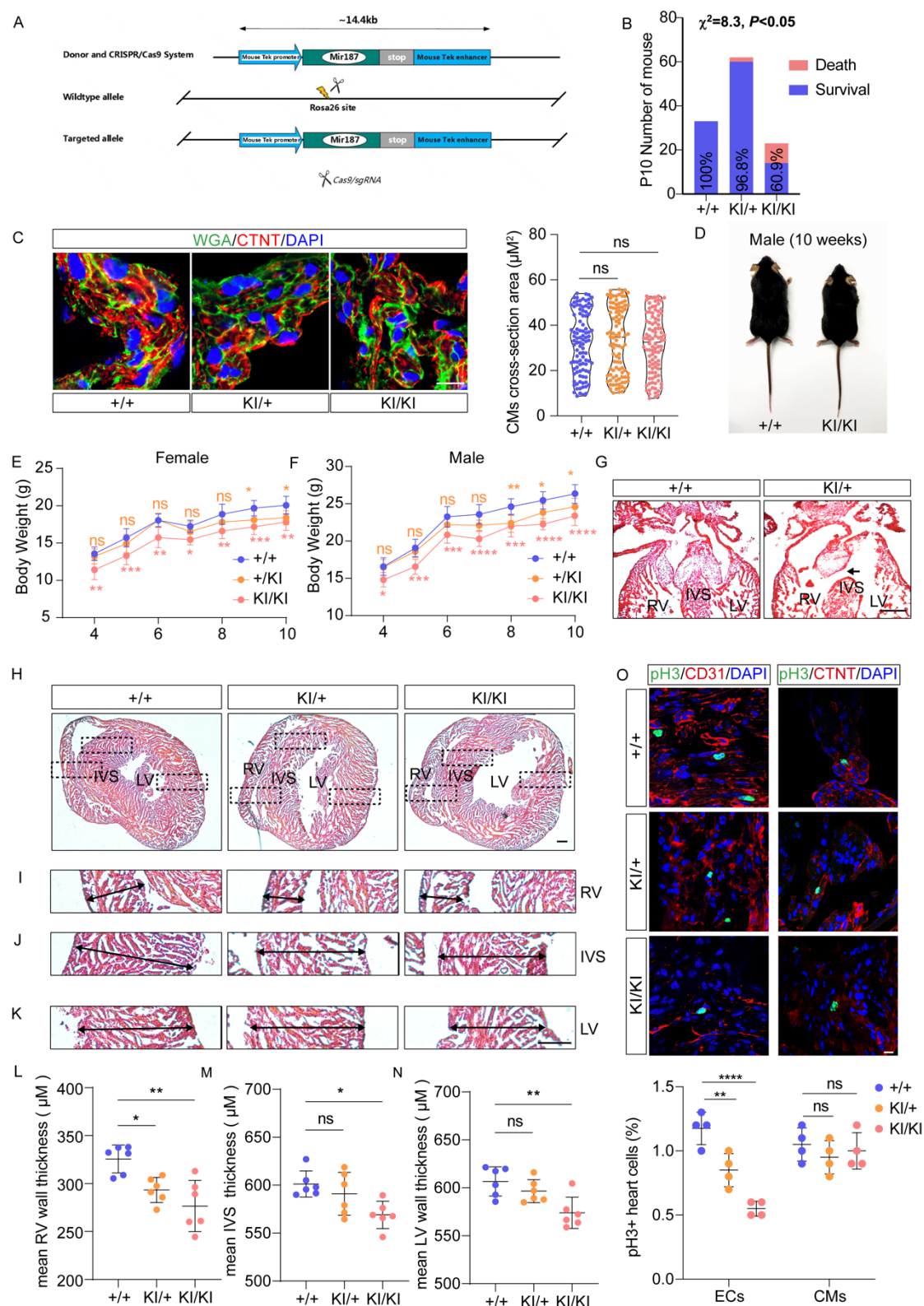


**Figure S3. Endothelial-specific mmu-miR-187 knock-in mice. (A)** Schematic illustration of strategy for knocking in TeK-mir-187 at the rosa26 locus. **(B)** The number of surviving and deceased normal controls and miR-187 KI mice after 10 days of birth. The survival rate is indicated in a specific column. Chi-square analysis is used to test whether the birth rate of miR-187 mice meets a 1:2:1 ratio. **(C)** Immunofluorescence staining of WGA and CTNT,



cardiac muscle cell marker (left) in heart sections from P0 neonatal mice and quantification (right) of the cross-section area of CMs (n=100). **(D)** Homozygous miR-187-KI mice are smaller in size than WT (+/+) littermates at week 10. **(E, F)** Homozygous female **(E)** and male **(F)** weighed less than WT from week 4 to week 10 (n=6). **(G)** H&E-stained heart sections from heterozygous mir-187 KI and control mice, displaying human CHD-like phenotypes, such as the control heart shows a normal septum; A mir-187 KI littermate of the animal in shows VSD at P0. **(H-K)** Double head arrows indicate the thickness of the compact myocardium of RV **(I)**, IVS **(J)** and LV **(K)**. **(L-N)** Quantification of the thickness of compact myocardium of RV **(L)**, IVS **(M)** and LV **(N)**. **(O)** Immunostainings for pH3, CD31 (endothelial cells marker) and CTNT (cardiomyocyte marker) show the number of heart mitotic cell at P0. DAPI was used for nuclear staining. The scale bars in (C), (G-K) and (O) are 20  $\mu$ m, 200  $\mu$ m and 10  $\mu$ m, respectively. Data are shown as means  $\pm$  SD. ns  $P > 0.05$ , \* $P < 0.05$ , \*\* $P < 0.01$ , \*\*\* $P < 0.001$ . Significance was determined by 1-way ANOVA (C, L-O), 2-way ANOVA (E and F) and Pearson's  $\chi^2$ -test (B).

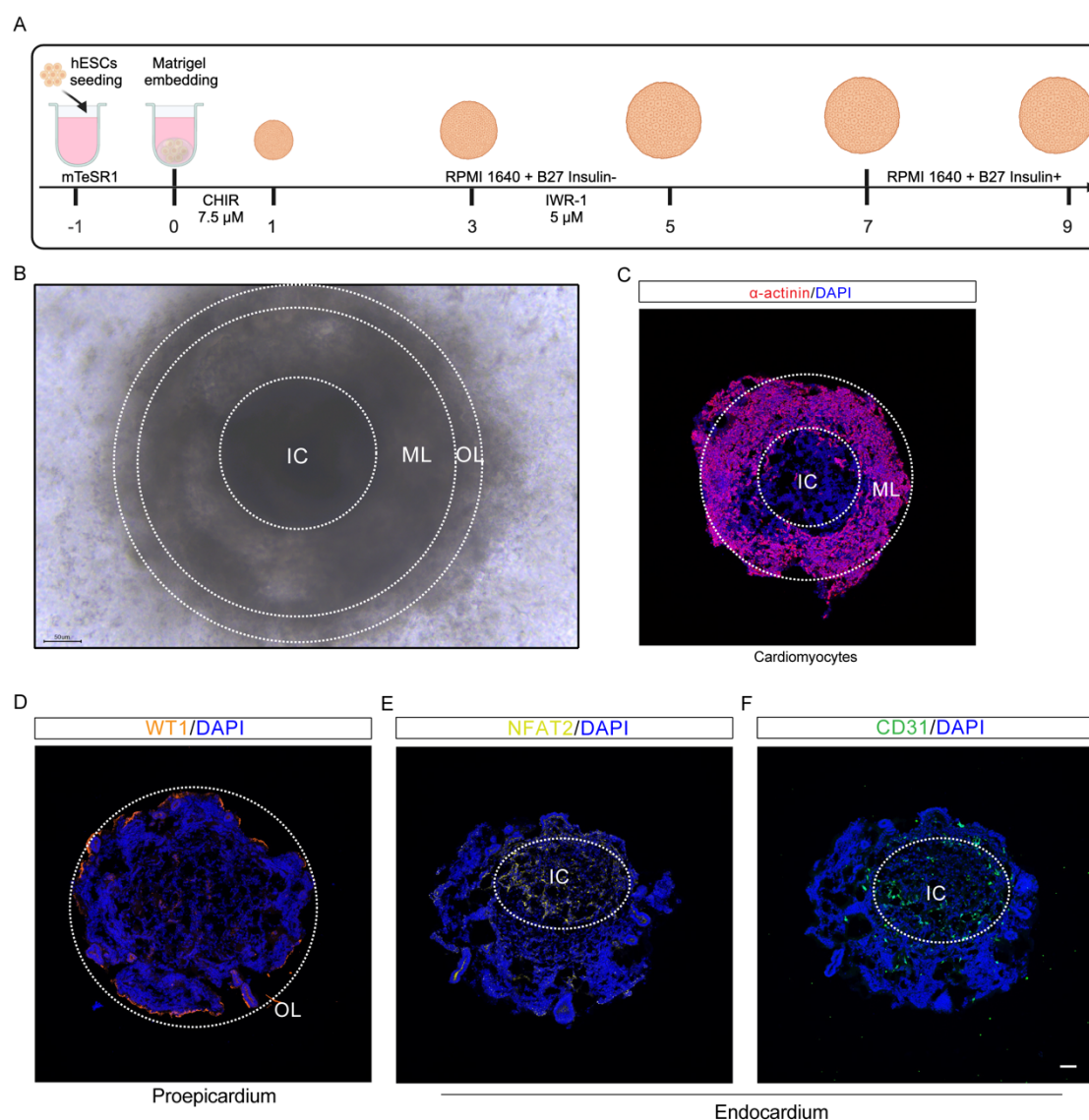


**Figure S4. Human heart-forming organoids are composed of a myocardial layer (ML) lined by endocardial inner core (IC) and surrounded by proepicardial outer layer (OL)**

**anlagen. (A)** The protocol for HFO formation involved embedding hESC aggregates individually in Matrigel and differentiating them using CHIR and IWR-1. **(B)** A typical hESC-derived HFO forming three layers: IC, ML and OL. **(C-F)** A section stained for cardiomyocyte ( $\alpha$ -actinin, **C**), proepicardium (WT1, **D**) and endocardium markers (NFAT2 and CD31, **E, F**) antibody. The scale bars in (B) and (C-F) are 50  $\mu$ m and 100  $\mu$ m, respectively.

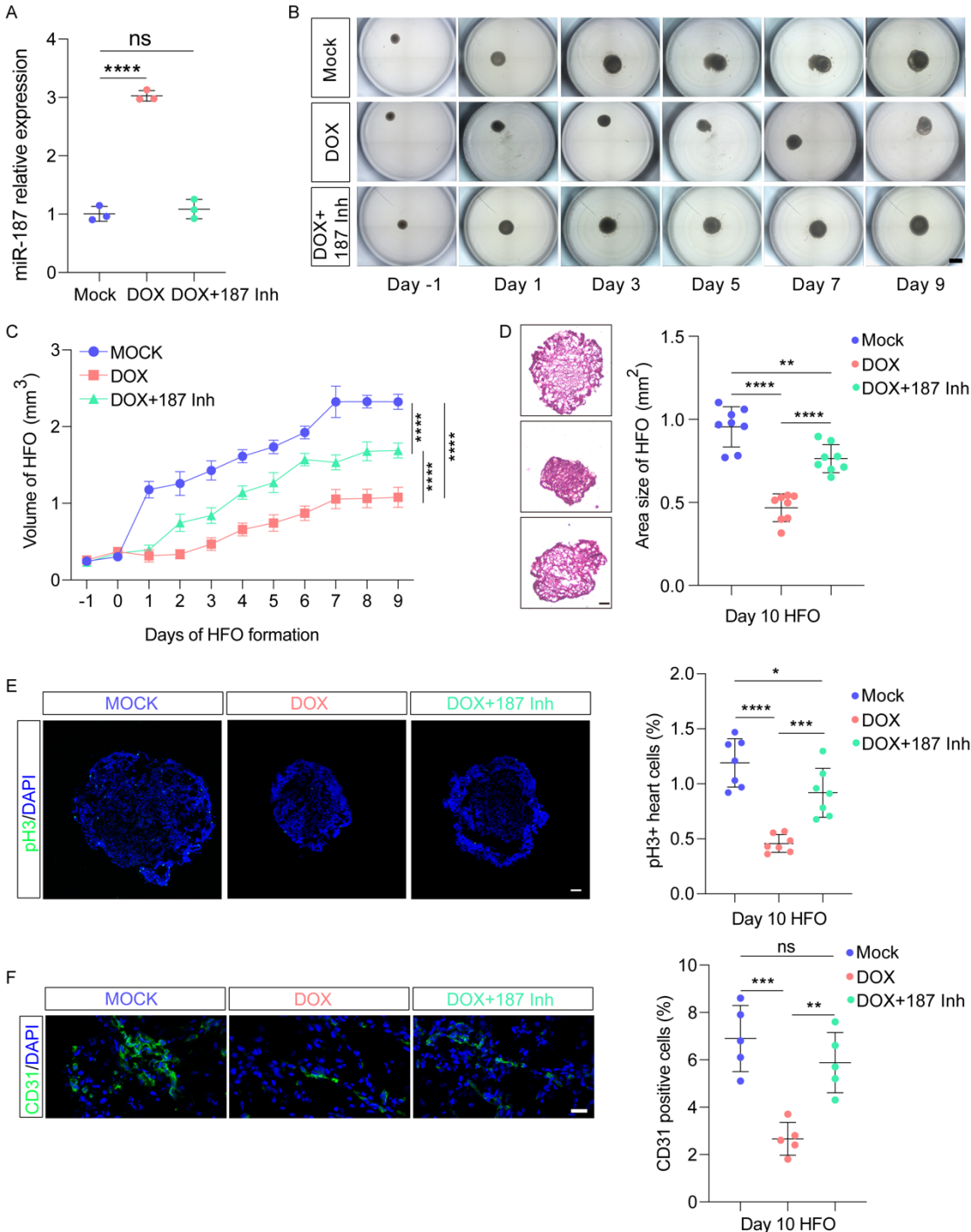


**Figure S5. Doxorubicin distributed human heart-forming organoids endothelial cell differentiation and mitosis by increasing miR-187. (A)** RT-qPCR detected miR-187 relative expression after DOX and DOX/miR-187 inhibitor treated in HFOs. **(B)** The figure shows the development of HFOs from day -1 until day 9 of mock, DOX and DOX/miR-187 inhibitor

---

differentiation. **(C)** Quantification of volume of HFOs (n=10) from day -1 until day 9 of mock, DOX and DOX/miR-187 inhibitor differentiation. **(D)** H&E staining (left) and quantification (n=8) (right) of area for mock, DOX and DOX/miR-187 inhibitor HFOs at day 10. **(E)** Immunostainings for pH3 (green, left) and quantification (n=8) (right) show the number of mitotic mock, DOX and DOX/miR-187 inhibitor HFO cells at day 10. **(F)** Representative immunofluorescence (green, left) and quantification (n=8) (right) staining of the endothelial cell marker CD31 in mock, miR-187 and miR-187/NIPBL HFO cells at day 10. DAPI was used for nuclear staining (blue). The scale bars in (B), (D, E) and (F) are 1 mm, 100  $\mu$ m and 20  $\mu$ m, respectively. Data are shown as means  $\pm$  SD. ns  $P > 0.05$ , \* $P < 0.05$ , \*\* $P < 0.01$ , \*\*\*\* $P < 0.0001$ . Significance was determined by 1-way ANOVA (A, D-F) and 2-way ANOVA (C).

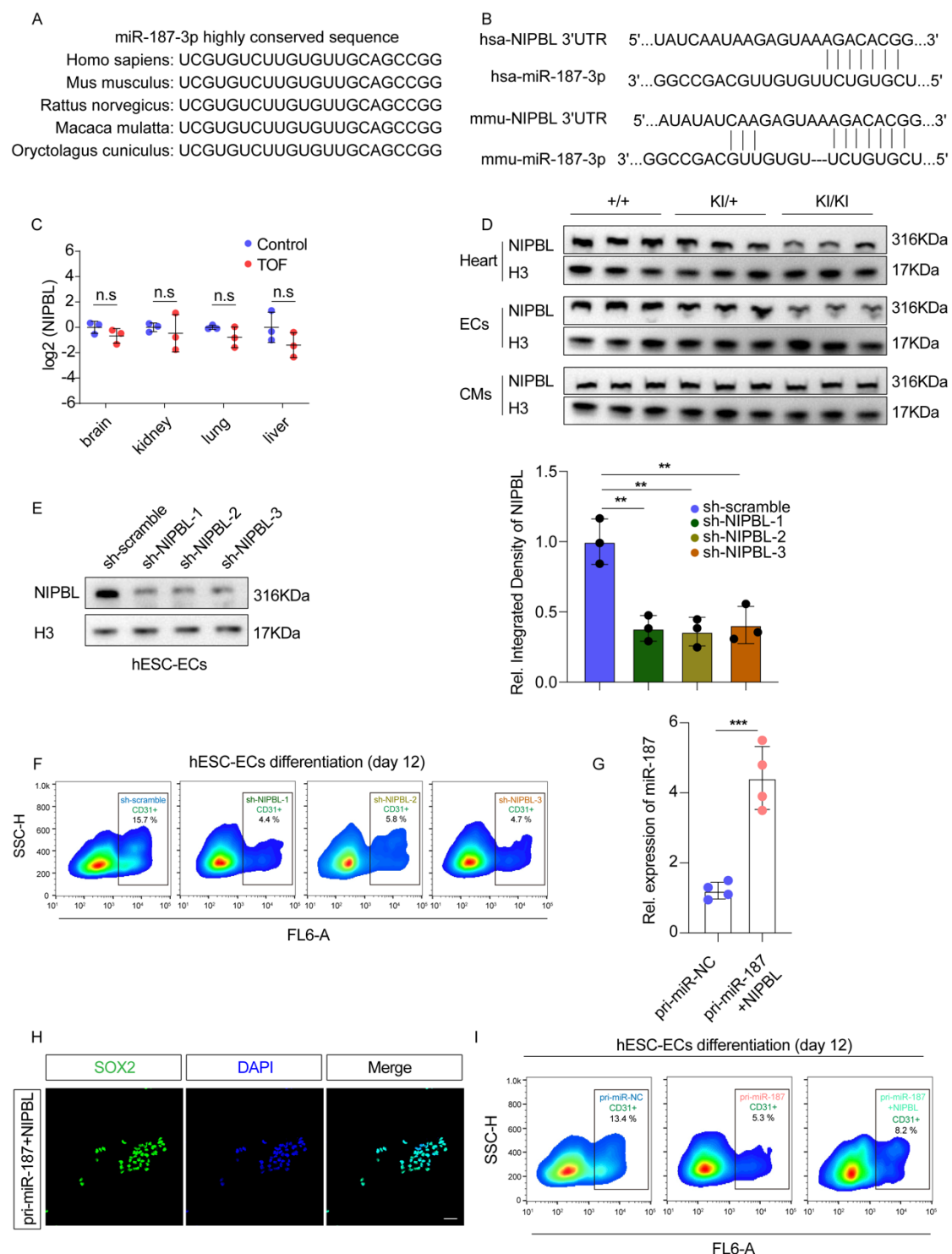
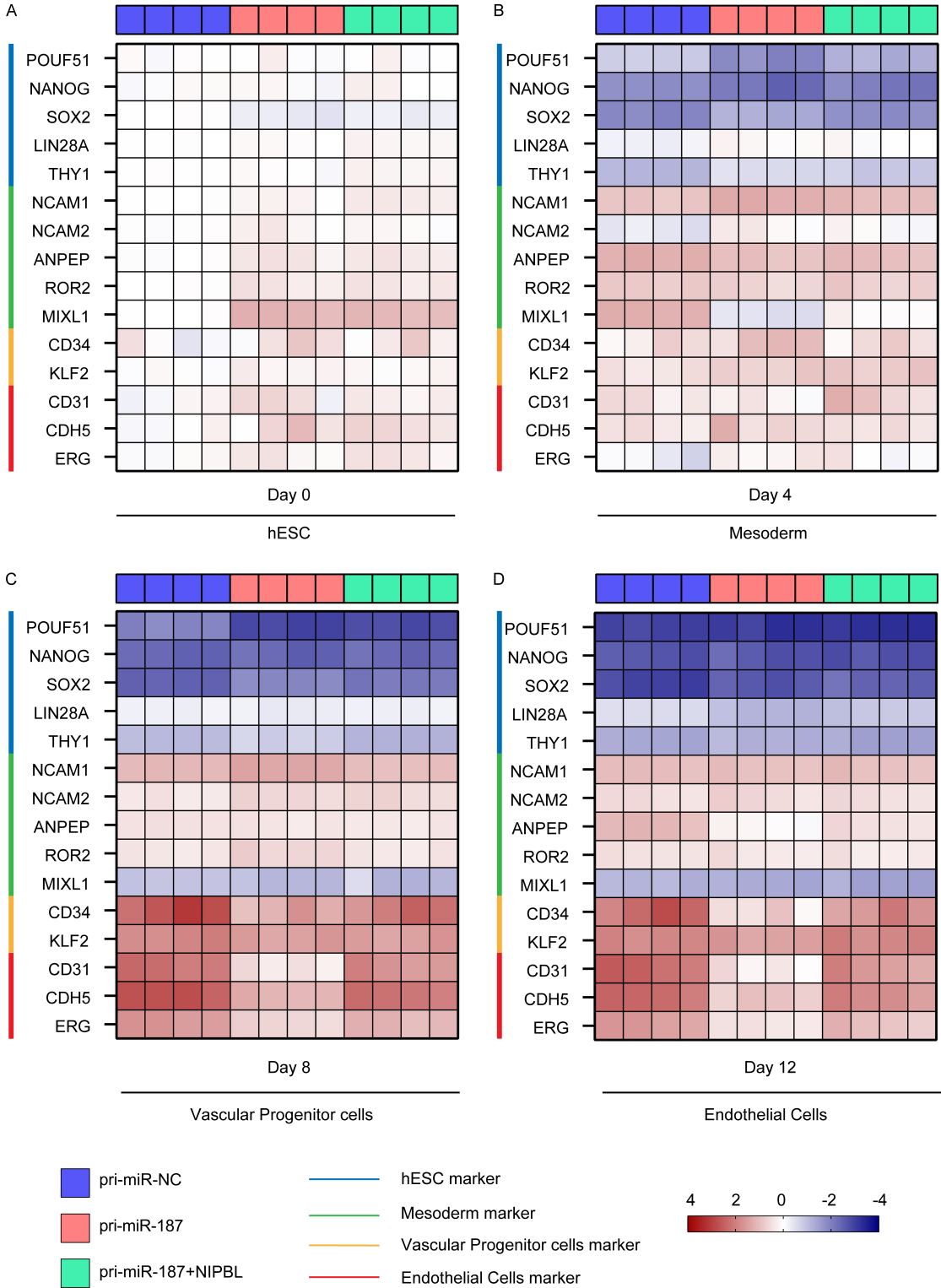


**Figure S6. miR-187 disturbs endothelial differentiation.** (A) The schematic depicts the conservation of the miR-187-3p sequence across various species. (B) The schematic illustrates the binding sequences of miR-187 and NIPBL 3'UTR in human and mouse. (C) RT-qPCR analyses of levels of NIPBL in brains, kidneys, livers and lungs of aborted fetuses with TOF (n=3) and normal controls (n=3). (D) Western blotting was performed to analyze the levels of Nipbl in whole hearts, cardiac endothelial cells, and cardiomyocytes of P0 mice with the indicated genotypes (n=3). H3 was used as a loading control. (E) Western blotting of NIPBL in hESC-ECs expressed sh-NIPBL-1, 2 and 3 or sh-scramble as indicated. H3 was used

1157 as a loading control. **(F, I)** FACS analysis of CD31 positive cells in hESC-ECs infection with sh-  
1158 NIPBL-1, 2, 3 (n=4) **(F)**, sh-scramble, pri-miR-187, pri-miR-187+NIPBL or scramble control  
1159 by lentivirus (n=4) **(I)**. **(G, H)** RT-qPCR analysis of miR-187 level (n=4) **(G)** and SOX2-  
1160 immunofluorescence staining for pluripotency marker SOX2 (green) **(H)** in hESCs infected  
1161 with miR-187/NIPBL or control virus. Scale bars in **(H)** are 50  $\mu$ m. Data are shown as means  
1162  $\pm$  SD. ns  $P > 0.05$ , \*\* $P < 0.01$ , \*\*\* $P < 0.001$ . Significance was determined by 1-way ANOVA  
1163 (C, E) and 2-tailed t test (G).



1164

**Figure S7. NIPBL recovered miR-187-mediated inhibition of endothelial differentiation.** (A-D) Heat map of RT-qPCR analyses of expression levels of various markers for hESC (A), mesoderm (B), vascular progenitor cells (C) and mature endothelial cells (D) during differentiation from hESCs to endothelial cells (n=4).

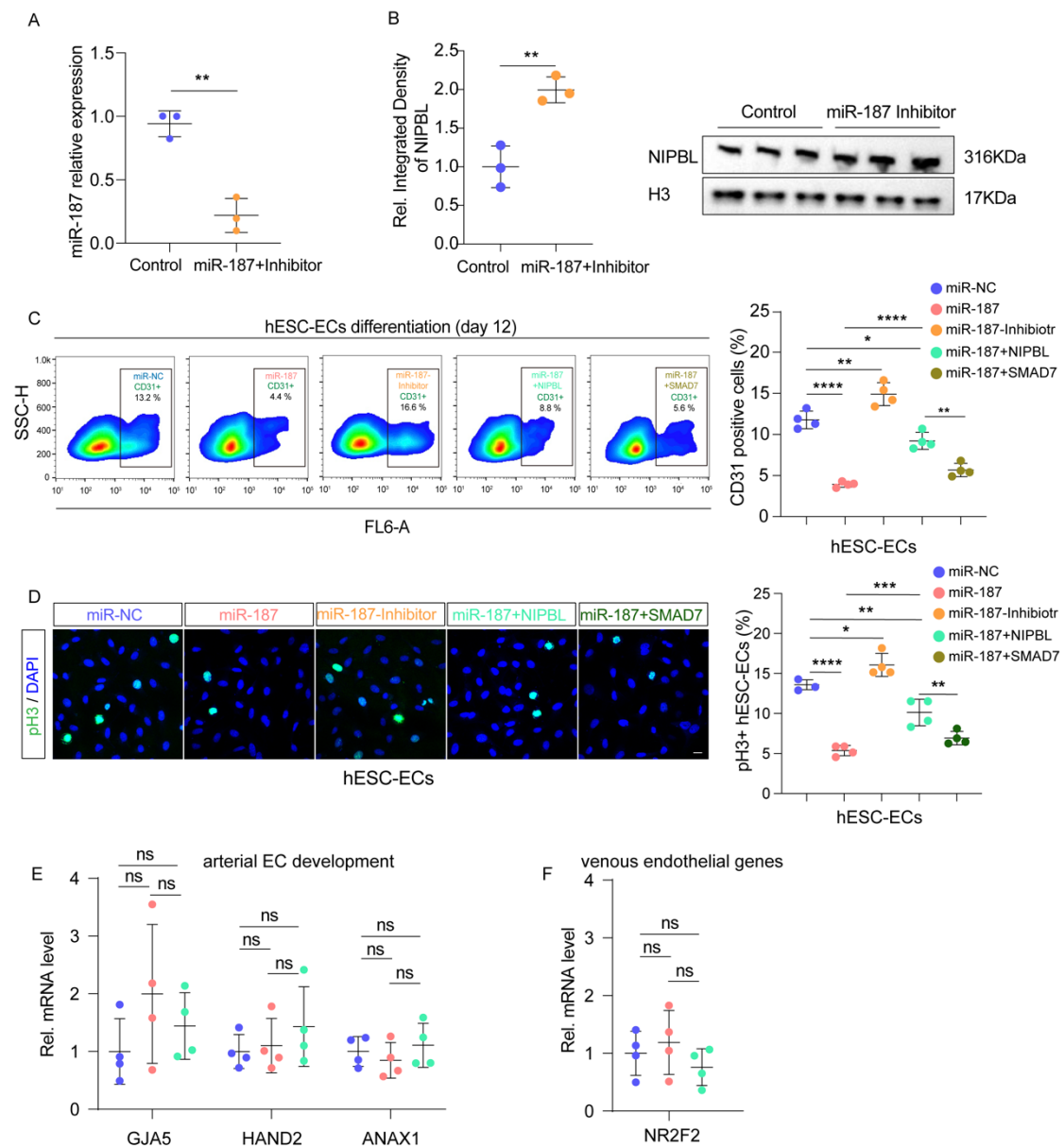


**Figure S8. miR-187 inhibits endothelial cell differentiation and mitosis.** (A,B) RT-qPCR and Western blotting were used to respectively measure the levels of miR-187 (A) and the protein expression of NIPBL (B) after adding a miR-187 inhibitor in hESC-ECs. (C, D) During hESC differentiation into hESC-ECs, miR-NC, miR-187, miR-187-inhibitor, miR-187/NIPBL, and miR-187/SMAD7 were overexpressed. FACS was used to quantify CD31-marked hESC-ECs as a measure of differentiation efficiency (C). Immunofluorescence was performed to assess the mitotic capability of pH3-marked hESC-ECs (D). (E, F) RT-qPCR analyses of expression levels of various markers for arterial EC development (E) and venous endothelial genes (F) (n=4). GAPDH was used as an internal control. The scale bars in (D) are 20  $\mu$ m. Data are shown as means  $\pm$  SD. ns  $P > 0.05$ , \* $P < 0.05$ , \*\* $P < 0.01$ , \*\*\* $P < 0.001$ ,



\*\*\*\* $P < 0.0001$ . Significance was determined by 1-way ANOVA (C-F) and 2-tailed t test (A and B).

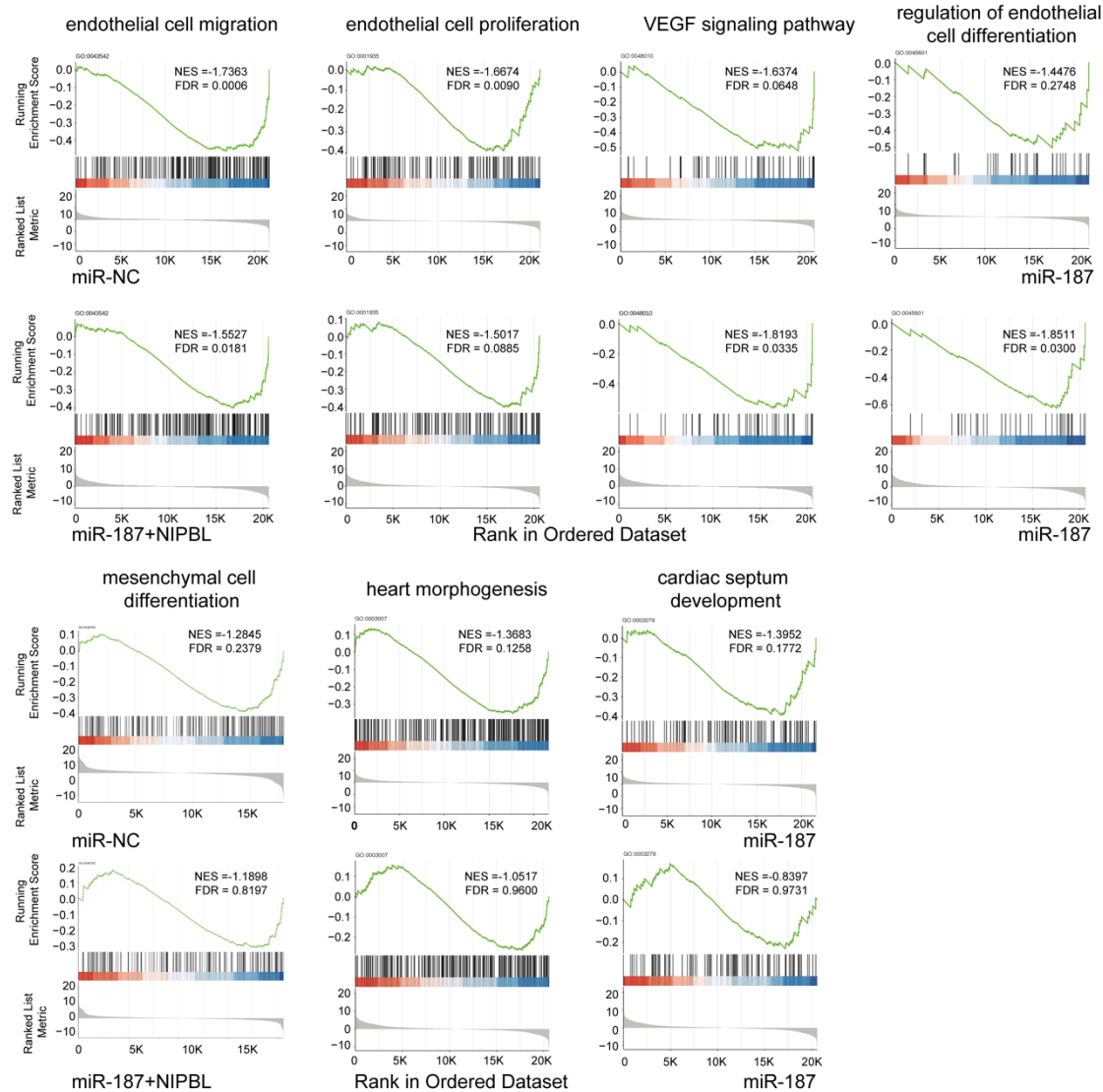


**Figure S9. miR-187/NIPBL axis inhibits endocardial gene expression.** Representative GSEA results for endothelial cell migration (GO:0043542), endothelial cell proliferation (GO:0001935), vascular endothelial growth factor receptor signaling pathway (GO:0048010), regulation of endothelial cell differentiation (GO:0045601), mesenchymal cell differentiation (GO:0048762), heart morphogenesis (GO:0003007) and cardiac septum development (GO:0003279) gene sets.

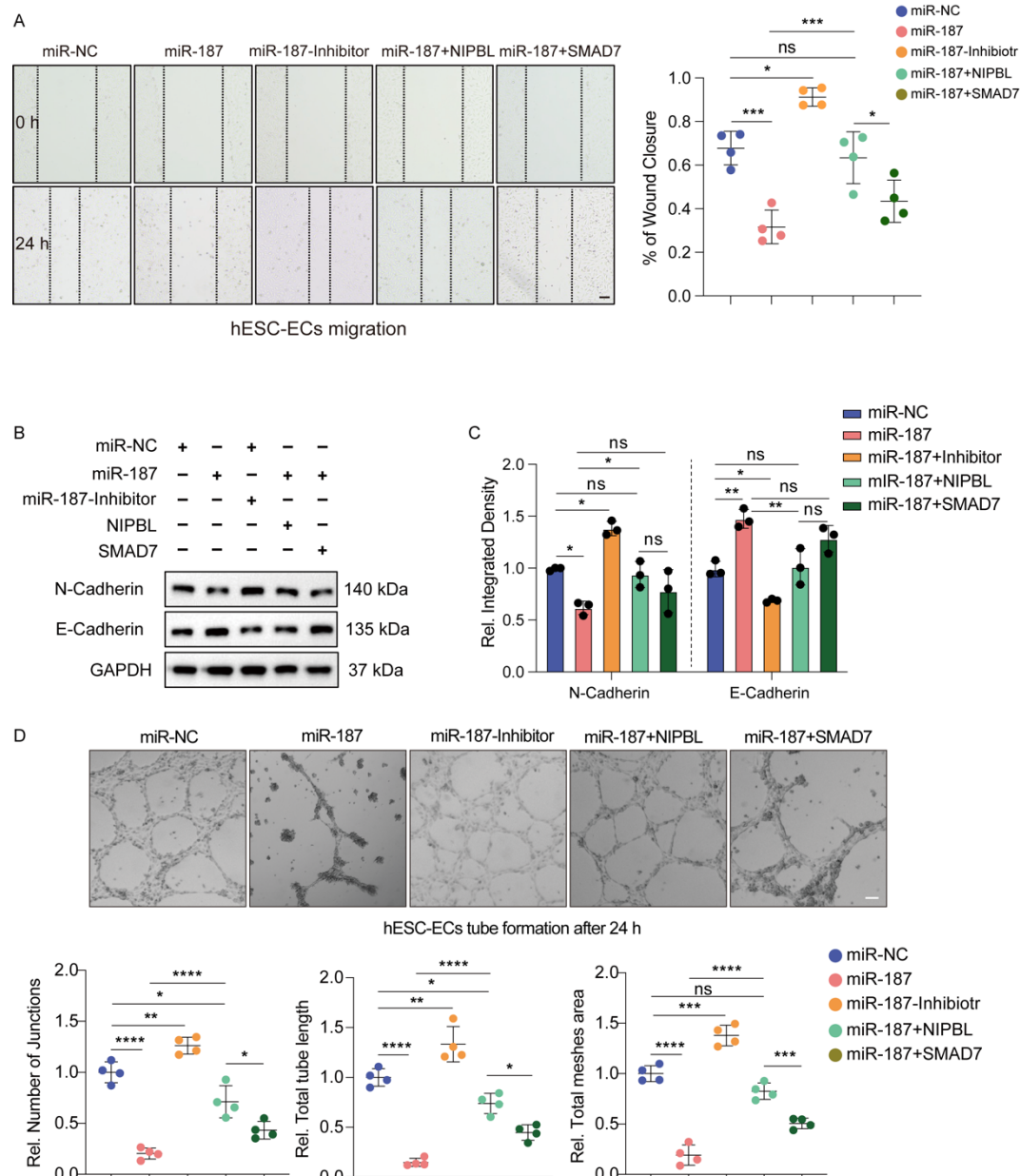


**Figure S10. miR-187 inhibits endothelial cell migration, epithelial to mesenchymal transition and tube formation. (A-D)** During hESC differentiation into hESC-ECs, miR-NC, miR-187, miR-187-inhibitor, miR-187/NIPBL, and miR-187/SMAD7 were overexpressed. **(A)** The migration ability was determined by the wound healing assays. The wound closure area was measured and quantified (n=4). **(B, C)** Western blotting analysis **(B)** and quantification **(C)** of protein levels of N-Cadherin and E-Cadherin (n=3). GAPDH was used as a loading control. **(D)** Tube formation assays revealed a marked reduction in tube formation by hESC-ECs transfected with miR-187 mimic (upper), quantified by assessing the number of tubes, nodes, and meshes (bottom) (n=4). The scale bars in **(A, D)** are and 100  $\mu$ m. Data are shown as means  $\pm$  SD. ns  $P > 0.05$ ,  $*P < 0.05$ ,  $**P < 0.01$ ,  $***P < 0.001$ ,  $****P < 0.0001$ . Significance was determined by 1-way ANOVA (A, C and D).





**Figure S11. NIPBL recovers delaying HFO formation induced by miR-187. (A-L)** The figure shows the development of HFOs from day -1 to day 10 of mock (A-L), miR-187 and miR-187/NIPBL differentiation.

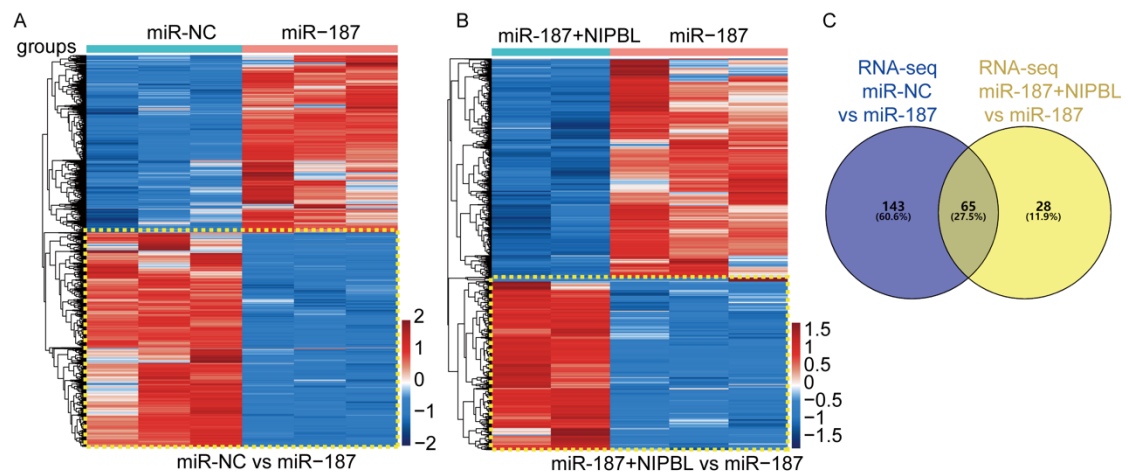


**Figure S12. RNA-Seq Screening of Differentially Expressed Genes in hESC-ECs**

**Influenced by miR-187 and NIPBL.** (A, B) Heat map of RNA-seq analyses of differentially expressed genes for pri-miR-NC-hESC-ECs vs pri-miR-187-hESC-ECs (A) and pri-miR-187/NIPBL-hESC-ECs vs pri-miR-187-hESC-ECs (B). (C) Schematic illustration of the screening approach for downstream genes of miR-187/NIPBL axis using miR-NC-hESC-ECs, miR-187-hESC-ECs and miR-187/NIPBL-hESC-ECs RNA-seq.

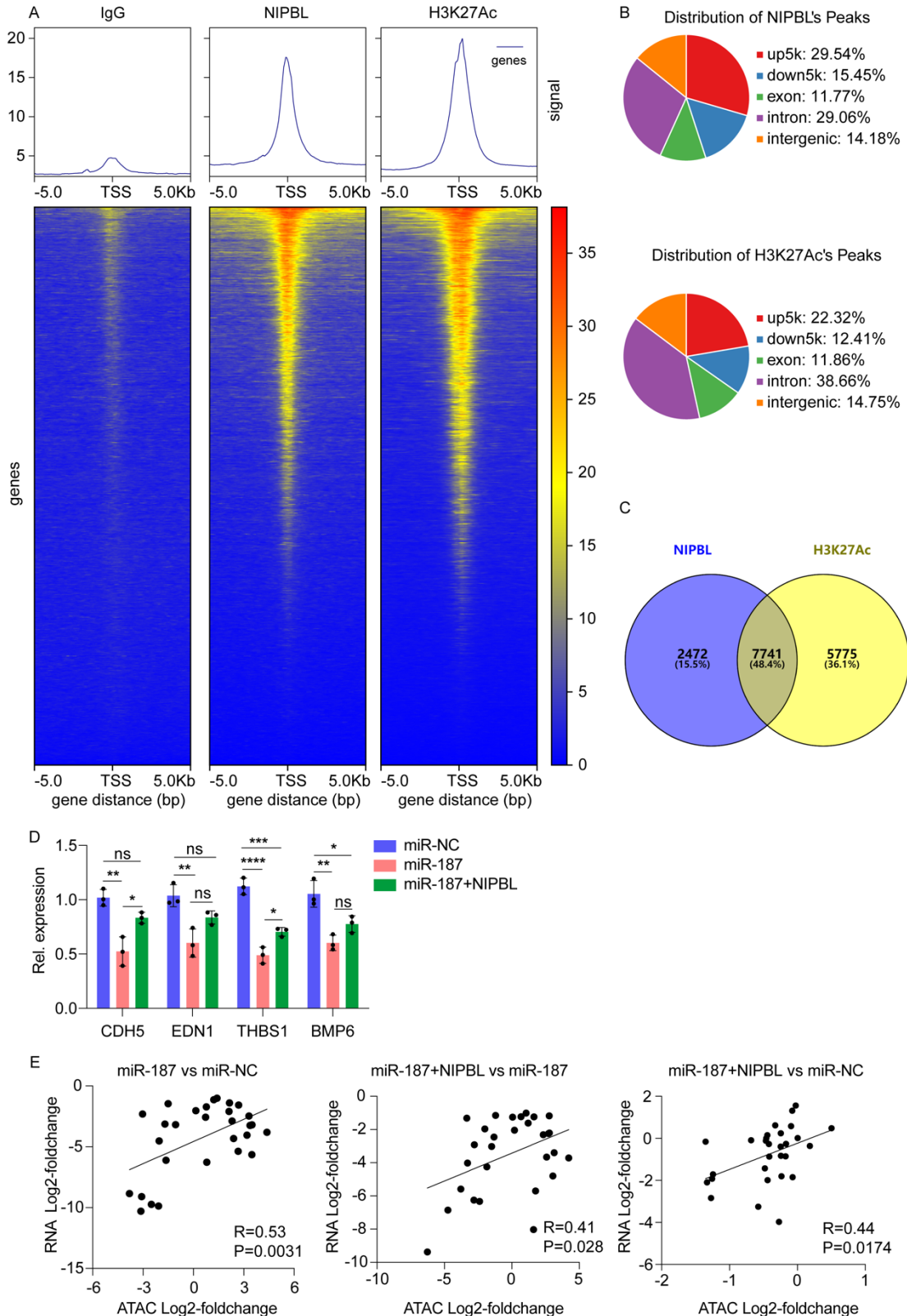


**Figure S13. miR-187/NIPBL axis inhibits endocardial gene chromatin accessibility. (A, B)** Density heatmaps **(A)** and distributions **(B)** of IgG-CUT&Tag, NIPBL-CUT&Tag and H3K27Ac-CUT&Tag in hESC-ECs. **(C)** Schematic illustration of the screening approach for downstream genes of miR-187/NIPBL axis using NIPBL, H3K27Ac CUT&TAG-seq. **(D)** Gene expression levels were detected by RNA-qPCR after exogenous miR-NC, miR-187, miR-187+NIPBL transfection in hESC-ECs. **(E)** The scatter plot depicts the correlation between RNA-seq and ATAC-seq data for 29 screened genes in hESC-ECs. Correlation coefficients and  $p$ -values are annotated in the figure. Data are shown as means  $\pm$  SD. \* $P < 0.05$ , \*\* $P < 0.01$ , \*\*\* $P < 0.001$ . Significance was determined by 1-way ANOVA (D).

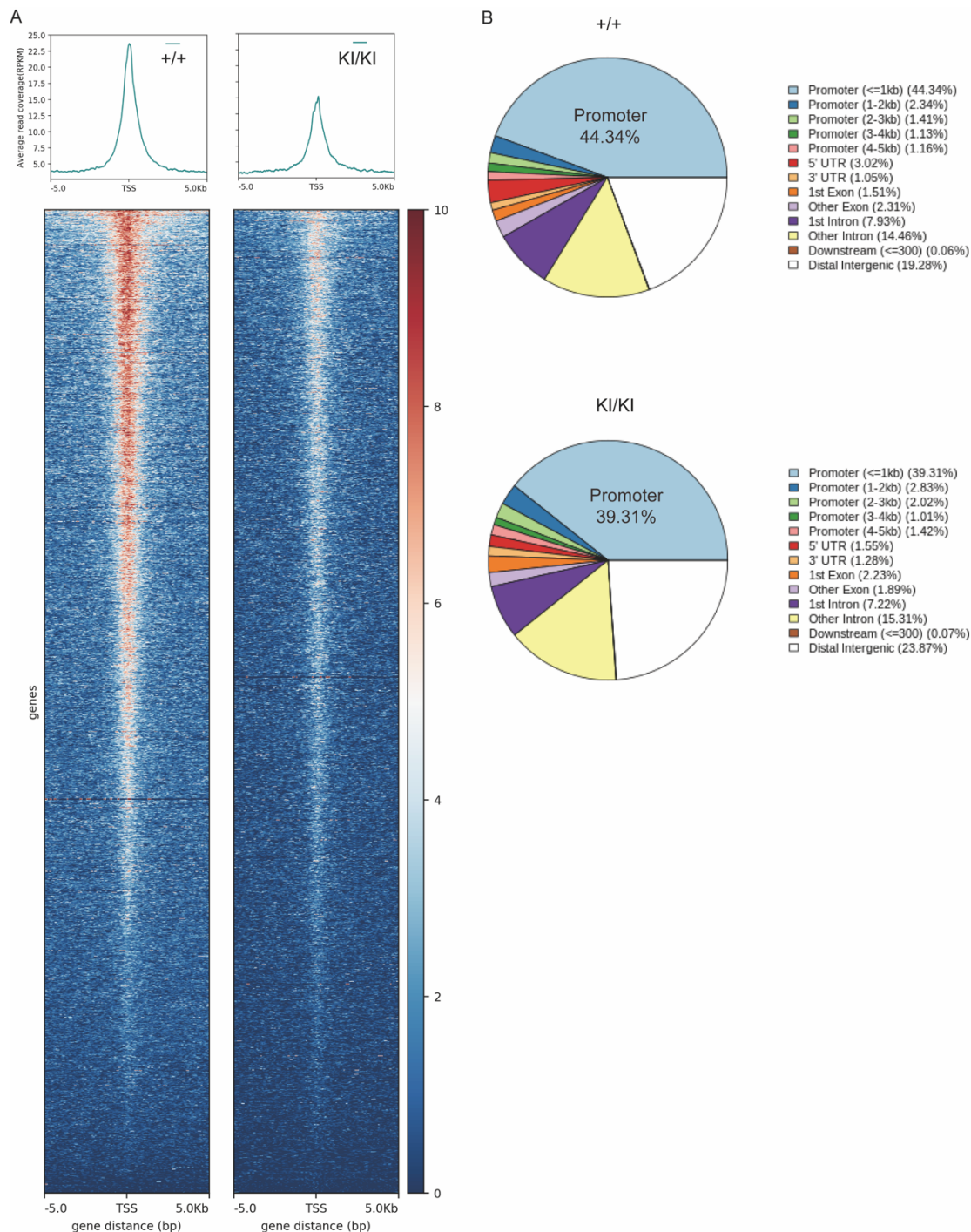




**Figure S14. Global chromatin accessibility changes in the endocardium of miR-187-KI mice.** (A) Average normalized ATAC-Seq signal intensity for all peaks changing in accessibility in WT and miR-187-KI mice (upper). Heatmap of signal distribution around ATAC-Seq peak summits for the same peaks (bottom). (B) Pie charts showing the distribution of genomic features among all peaks in the endocardium cardiac endothelial cells of miR-187-KI mice.

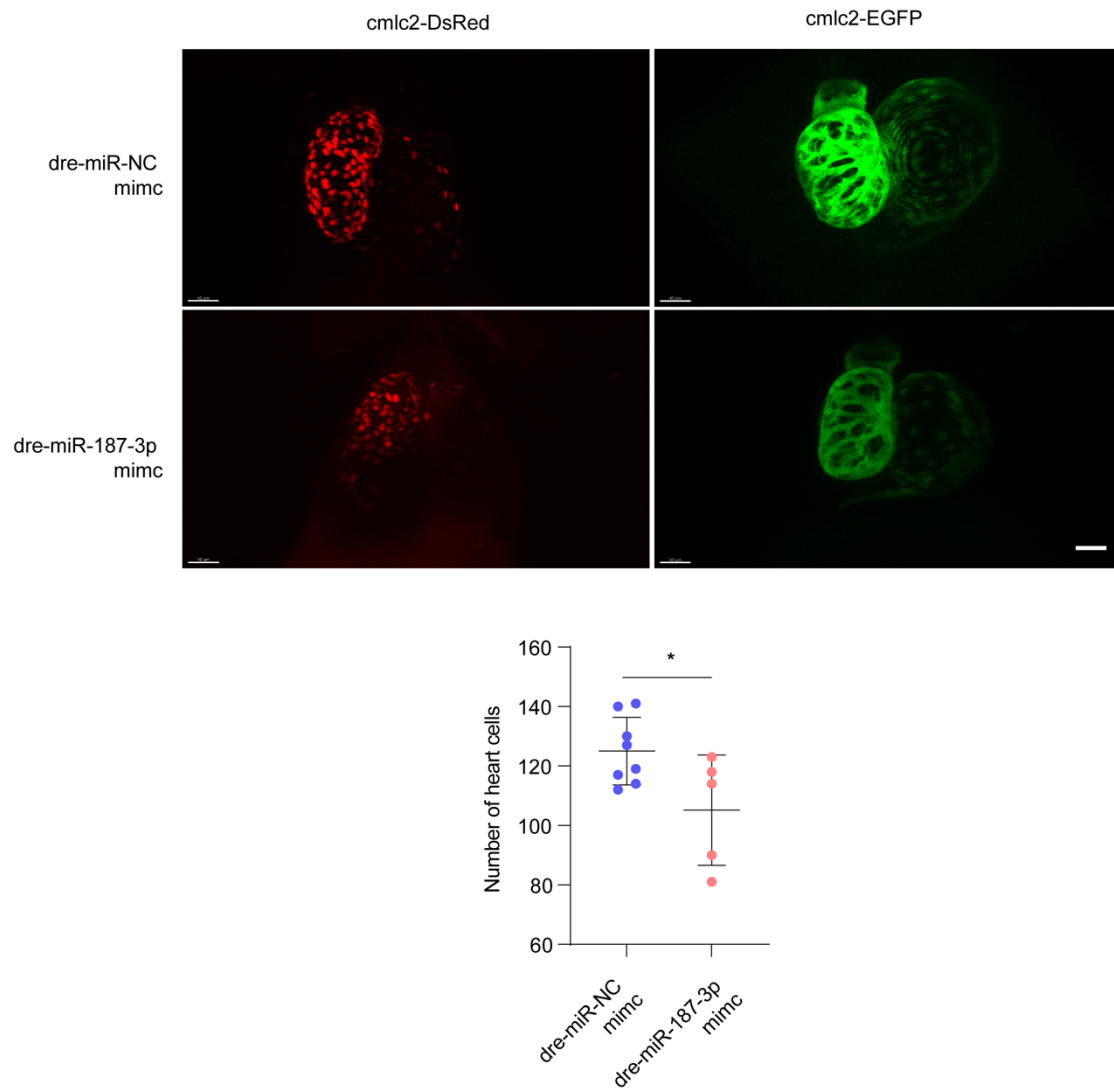


**Figure S15. dre-miR-187 reduces the number of heart cells in zebrafish.** Images (upper) and quantification (bottom) of hearts cells in cmlc2-DsRed and cmlc2-EGFP zebrafish at 72 hpf. Significance was determined by 2-tailed t test.

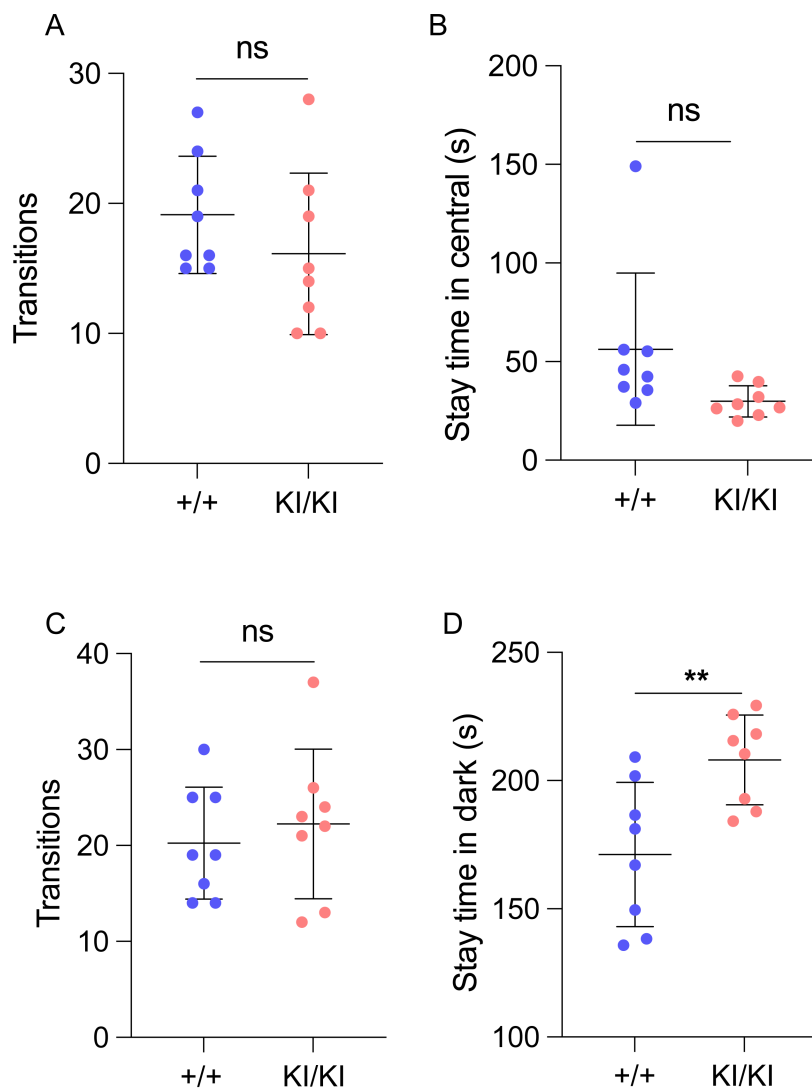


**Figure S16. miR-187 KI mice display anxiety-like behavior.** (A, B) Transitions of mice between peripheral and central zones (A) and duration of time spent in the central zone during the open field test (B). (C, D) Transition frequency between light and dark compartments (C) and time spent in the dark chamber (D). Significance was determined by 2-tailed t test (A-D).